J. Fluid Mech. (2010), *vol.* 660, *pp.* 499–526.
doi:10.1017/S002211201000279X

Effect of compressibility on the global stability of axisymmetric wake flows

P. MELIGA[1]†, D. SIPP[1] AND J.-M. CHOMAZ[2]

[1]ONERA/DAFE, 8 rue des Vertugadins, 92190 Meudon, France

[2]LadHyX, CNRS-Ecole Polytechnique, 91128 Palaiseau, France

(Received 10 August 2009; revised 11 May 2010; accepted 12 May 2010;
first published online 19 August 2010)

We study the linear dynamics of global eigenmodes in compressible axisymmetric wake flows, up to the high subsonic regime. We consider both an afterbody flow at zero angle of attack and a sphere, and find that the sequence of bifurcations destabilizing the axisymmetric steady flow is independent of the Mach number and reminiscent of that documented in the incompressible wake past a sphere and a disk (Natarajan & Acrivos, *J. Fluid Mech.*, vol. 254, 1993, p. 323), hence suggesting that the onset of unsteadiness in this class of flows results from a global instability. We determine the boundary separating the stable and unstable domains in the (M, Re) plane, and show that an increase in the Mach number yields a stabilization of the afterbody flow, but a destabilization of the sphere flow. These compressible effects are further investigated by means of adjoint-based sensitivity analyses relying on the computation of gradients or sensitivity functions. Using this theoretical formalism, we show that they do not act through specific compressibility effects at the disturbance level but mainly through implicit base flow modifications, an effect that had not been taken into consideration by previous studies based on prescribed parallel base flow profiles. We propose a physical interpretation for the observed compressible effects, based on the competition between advection and production of disturbances, and provide evidence linking the stabilizing/destabilizing effect observed when varying the Mach number to a strengthening/weakening of the disturbance advection mechanism. We show, in particular, that the destabilizing effect of compressibility observed in the case of the sphere results from a significant increase of the backflow velocity in the whole recirculating bubble, which opposes the downstream advection of disturbances.

Key words: compressible flows, instability, wakes/jets

1. Introduction

Axisymmetric wakes have been studied experimentally and numerically for different geometries of revolution (Mair 1965; Achenbach 1974; Fuchs, Mercker & Michel 1979). It has generally been acknowledged that this class of flows is dominated by an instability of the helical mode, resulting in the low-frequency shedding of large-scale coherent structures. In the context of afterbody flows, this vortex shedding is detrimental to the engineering application, as it may increase drag and cause flow-induced vibrations, resulting in fluctuating dynamic loads whose magnitude can be critical during the transonic phase of flight. We consider here a compressible

† Email address for correspondence: philippe.meliga@epfl.ch

afterbody flow at moderate Reynolds number and at a Mach number $M = 0.5$, a parameter setting which may be of practical interest for the low-density flows encountered in the stratosphere by high-altitude rockets and re-entry vehicles. In this range of Reynolds numbers, the vortex-shedding activity has been linked to an instability of helical modes of azimuthal wavenumbers $m = \pm 1$ (Siegel & Fasel 2001; Seidel *et al.* 2008). For the higher Reynolds numbers found at lower altitudes, vortex shedding persists as a coherent large-scale phenomenon superimposed on the turbulent flow field (Achenbach 1972; Taneda 1978; Deprés, Reijasse & Dussauge 2004), which suggests that the present results rigorously derived at moderate Reynolds numbers can carry over as a first step towards the turbulent case.

We consider two model geometries of blunt and bluff bodies, namely an axisymmetric blunt-based afterbody modelling an ideal rocket shape and a sphere. An eigenvalue solution of any compressible stability problem depends on the base flow profiles and on the Mach number, the base flow itself being an implicit function of the Mach number. When the latter is varied, compressible effects are thus simultaneously at work at the perturbation and the base flow levels, since the Mach number is modified both in the disturbance and the base flow equations. The effect of compressibility on the stability of shear flows has been so far addressed in the framework of the local theory of parallel flows (Michalke 1971; Pavithran & Redekopp 1989, amongst others). The most widely used approximation is to prescribe analytical base flow profiles satisfying the inviscid Navier–Stokes equations. In this case, the base flow is independent of the Mach number, meaning that this approach is relevant only to assessment of the effect of compressibility at the perturbation level. Another approximation is to add the Crocco–Busemann relation derived from the steady boundary-layer equations (Schlichting 1978) to include a Mach squared compressible correction in the density and temperature profiles (Jackson & Grosch 1990; Jendoubi & Strykowski 1994). This allows recovery of the effect of compressibility on the base flow thermodynamic variables. Still, it fails to consider its effect on the base flow velocity profiles, which turns out to be of crucial importance for the non-parallel wake flows considered here, as will be shown in the following.

The present study uses the framework of the global stability of non-parallel flows, i.e. flows that are inhomogeneous in both the cross-stream and the streamwise directions (Jackson 1987), for which the base flow underlying the stability analysis is first computed as a solution of the compressible Navier–Stokes equations, without any other approximation. In the incompressible regime, Natarajan & Acrivos (1993) have shown that the axisymmetric solution prevailing at low Reynolds numbers is generically unstable to a steady and a time-periodic global mode. The onset of unsteadiness in the real flow ultimately results from the leading-order nonlinear interaction of these concomitantly unstable modes (Fabre, Auguste & Magnaudet 2008; Meliga, Chomaz & Sipp 2009*a*): the sequence of bifurcation undergone by the real flow then involves the destabilization of the steady three-dimensional branch by an antisymmetric or a symmetric perturbation made of the superposition of two counter-rotating oscillating modes with different phases. This competition between modes is not within the scope of the present study, which deals instead with the effect of compressibility on the oscillating mode, believed to trigger the onset of the periodic regime at higher Reynolds numbers (Ormières & Provansal 1999; Tomboulides & Orszag 2000). Increased computer capacities now make it possible to apply this approach to the compressible regime, where a number of computational issues arise (see Crouch, Garbaruk & Magidov 2007 or Crouch *et al.* 2009 on the shock-induced buffet over a two-dimensional airfoil, Brès & Colonius 2008 on the flow over an open

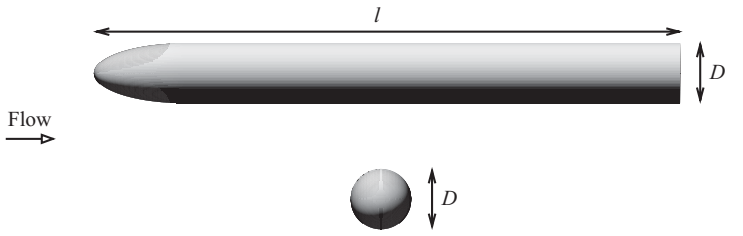

FIGURE 1. Schematic of the configurations under study. (*a*) Slender body of revolution of diameter D and total length $l = 9.8D$. (*b*) Sphere of diameter D.

cavity, Robinet 2007 on shock wave/boundary-layer interactions or Mack, Schmid & Sesterhenn 2008 on the flow around a swept parabolic body).

We develop a gradient-based sensitivity formalism for the study of compressible non-parallel flows. Compressible effects are viewed as an input/output sensitivity problem relying on the evaluation of the gradient of an eigenvalue (output) with respect to small modifications of the Mach number (input). Emphasis is put on the role of the base flow in the perturbation dynamics, as we generalize to compressible flows the sensitivity formalism originally formulated for parallel flows by Bottaro, Corbett & Luchini (2003) and Hwang & Choi (2006), and recently extended to spatially developing flows by Marquet, Sipp & Jacquin (2008). By investigating how the growth rate of an unstable mode is affected by changes in the shape of the base flow profiles, this analysis is appropriate to theoretical investigation of the mechanisms leading the instability. We use here adjoint methods to compute the gradients of interests by solving only once the state and adjoint problems. As will be shown, such an approach requires a relatively 'low' computational cost and allows us to provide physical interpretations for the observed effects by splitting a given gradient into the sum of production, streamwise advection and cross-stream advection terms.

The paper is organized as follows. The flow configuration and numerical method are presented in § 2. The base flow and disturbance equations are solved in § 3, where we investigate the impact of compressibility on the bifurcating modes. Section 4 presents a brief summary of the adjoint-based sensitivity formalism encompassing small modifications of the Mach number. The observed compressibility effects are ultimately discussed in § 4.3, where we show that the interpretations admitted up to now are not relevant to the case of wake flows. A physical interpretation is proposed in Section 5, in terms of a competition between the advection and production of disturbances.

2. Flow configuration and theoretical formulation

We investigate the stability of the axisymmetric flow developing in the compressible regime past two model geometries of revolution, namely the afterbody and the sphere shown in figure 1. The afterbody models a rocket shape, with a blunt trailing edge of diameter D placed into a uniform flow at zero angle of attack (Mair 1965; Weickgenannt & Monkewitz 2000), and is identical to that experimentally investigated by Sevilla & Martínez-Bazàn (2004), with a total length $l = 9.8D$ and an ellipsoidal nose of aspect ratio 3 : 1. The problem is formulated using a standard cylindrical coordinate system (r, θ, z) of axis Γ_a, whose origin is taken at the centre of the base for the afterbody, and at the centre of the body for the sphere.

2.1. *Governing equations*

The fluid is a non-homogeneous compressible perfect gas with constant specific heat c_p, thermal conductivity κ and dynamic viscosity μ, related by a unit Prandtl number. The fluid motion is described by the state vector $\boldsymbol{q}=(\varrho,\boldsymbol{u},\Theta,p)^T$, where the superscript T designates the transpose, ϱ is the density, Θ is the temperature, p is the pressure and $\boldsymbol{u}=(u,v,w)^T$ is the three-dimensional velocity field with u, v and w its radial, azimuthal and streamwise components, respectively. The state vector $\boldsymbol{q}$ obeys the unsteady compressible Navier–Stokes equations, thus leading to a set of six nonlinear equations (continuity, momentum, internal energy and perfect gas) formulated in non-conservative variables as

$$\partial_t\varrho+\varrho\boldsymbol{\nabla}\cdot\boldsymbol{u}+\boldsymbol{u}\cdot\boldsymbol{\nabla}\varrho=0, \tag{2.1a}$$

$$\varrho\partial_t\boldsymbol{u}+\varrho\boldsymbol{\nabla}\boldsymbol{u}\cdot\boldsymbol{u}+\frac{1}{\gamma M^2}\boldsymbol{\nabla}p-\frac{1}{Re}\boldsymbol{\nabla}\cdot\boldsymbol{\tau}(\boldsymbol{u})=\boldsymbol{0}, \tag{2.1b}$$

$$\varrho\partial_t\Theta+\varrho\boldsymbol{u}\cdot\boldsymbol{\nabla}\Theta+(\gamma-1)p\boldsymbol{\nabla}\cdot\boldsymbol{u}-\gamma(\gamma-1)\frac{M^2}{Re}\,\boldsymbol{\tau}(\boldsymbol{u}):\boldsymbol{d}(\boldsymbol{u})-\frac{\gamma}{PrRe}\nabla^2\Theta=0, \tag{2.1c}$$

$$p-\varrho\Theta=0, \tag{2.1d}$$

with $\boldsymbol{d}(\boldsymbol{u})$ and $\boldsymbol{\tau}(\boldsymbol{u})$ the strain and stress tensors defined as

$$\boldsymbol{d}(\boldsymbol{u})=\frac{1}{2}(\boldsymbol{\nabla}\boldsymbol{u}+\boldsymbol{\nabla}\boldsymbol{u}^T),\quad \boldsymbol{\tau}(\boldsymbol{u})=-\frac{2}{3}(\boldsymbol{\nabla}\cdot\boldsymbol{u}\ )\boldsymbol{I}+2\boldsymbol{d}(\boldsymbol{u}). \tag{2.2}$$

Note that a different set of equations can be used, if the internal energy equation is replaced by its total energy or entropy counterpart. Equations (2.1) have been made non-dimensional using the body diameter D and the upstream quantities W_∞, ϱ_∞, Θ_∞ and p_∞ as respective velocity, density, temperature and pressure scales, and the Reynolds and Mach numbers are defined as

$$Re=\frac{\varrho_\infty DW_\infty}{\mu},\quad M=\frac{W_\infty}{\sqrt{\gamma R_g\Theta_\infty}}, \tag{2.3}$$

with R_g the ideal gas constant. For the afterbody flow, the Reynolds number for transition to turbulence in the developing boundary layer is $Re\simeq 12\,000$, as estimated from Weickgenannt & Monkewitz (2000). The Reynolds numbers prevailing here being such that $Re<1500$, we assume that the boundary layer thus remains laminar up to the trailing edge. This assumption also holds for the sphere, for which the transition occurs at Reynolds numbers $Re\gtrsim 800$ (Tomboulides & Orszag 2000).

2.2. *Numerical method*

From now on, all governing equations are given as formal relations between differential operators. Equations (2.1) are thus conveniently written as

$$\mathscr{B}(\boldsymbol{q})\partial_t\boldsymbol{q}+\mathscr{M}(\boldsymbol{q},\mathscr{G})=\boldsymbol{0}, \tag{2.4}$$

where $\mathscr{B}$ and $\mathscr{M}$ are differential operators and $\mathscr{G}$ is a set of relevant control parameters made here of the Reynolds and Mach numbers only (in particular, the angle of attack remains zero throughout the study). In the following, one must distinguish between the complete form of these operators, defined for the state vector $\boldsymbol{q}=(\varrho,\boldsymbol{u},\Theta,p)^T$, and their reduced forms defined for the state vector $\boldsymbol{q}=(\varrho,\boldsymbol{u},\Theta)^T$, which can be straightforwardly deduced by replacing the pressure terms by their expressions arising from the perfect gas state equation. The complete form is more suitable to the presentation of the theoretical framework, whereas the reduced form is used in the

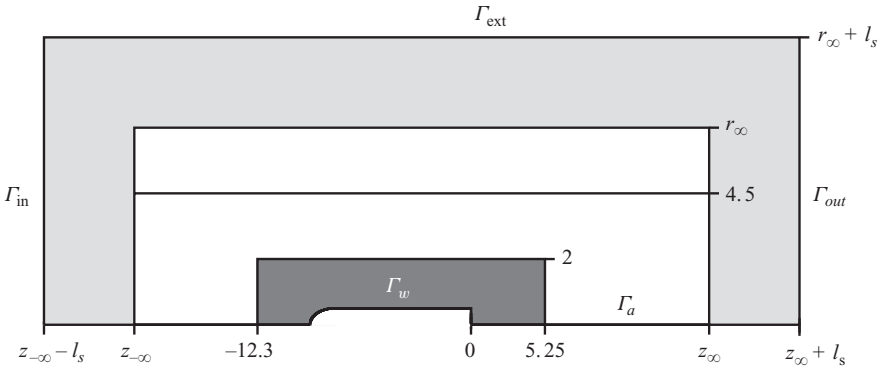

FIGURE 2. Schematic of the computational domain Ω for the afterbody flow: $z_{-\infty}$, z_∞ and r_∞ denote the location of the physical inlet, outlet and lateral boundaries. This physical domain is padded with a sponge zone of width l^s, shown as the light grey shaded area. The inner solid lines delimit regions characterized by different vertex densities. The dark grey shaded area corresponds to the near-wake domain Ω_{in} used to normalize the eigenmodes.

numerics as it requires smaller computational resources. To ease the reading, we omit voluntarily the difference between both forms, the choice of the relevant one being clear from the context. The complete form of all operators is detailed in Appendix D.

The choice of the boundary conditions is crucial in compressible flows. In order to apply appropriate far-field conditions, the body is enclosed into two concentric cylinders defined as

$$r \leqslant r_\infty \quad \text{and} \quad z_{-\infty} \leqslant z \leqslant z_\infty \qquad \text{(inner cylinder)}, \tag{2.5a}$$

$$r \leqslant r_\infty + l_s \quad \text{and} \quad z_{-\infty} - l_s \leqslant z \leqslant z_\infty + l_s \qquad \text{(outer cylinder)}. \tag{2.5b}$$

The inner enclosing cylinder corresponds to the footprint of the computational domain that would have been used for an incompressible flow, whereas the outer cylinder defines the location of the inlet, outlet and external boundaries (denoted Γ_{in}, Γ_{out} and Γ_{ext}, respectively) in the numerics. In the domain enclosed between the cylinders, shown as the light grey shaded area in figure 2, all fluctuations are progressively damped to negligible levels through artificial dissipation, as the Reynolds number is smoothly decreased from its value defined in (2.3) to the small value $Re_s = 0.1$ at the boundary of the computational domain. The purpose of such sponge regions is to minimize numerical-box-size effects by gradually attenuating all vortical and acoustic fluctuations before they reach the boundary of the domain (Colonius 2004). The Reynolds number in all equations should therefore be replaced by a 'computational' Reynolds number $\widetilde{Re}$ defined by $\widetilde{Re}(r, z) = Re$ in the inner cylinder, and

$$\widetilde{Re}(r, z) = Re + (Re_s - Re)\zeta(z, z_\infty) \quad \text{if} \quad r \leqslant r_\infty \quad \text{and} \quad z > z_\infty, \tag{2.6a}$$

$$\widetilde{Re}(r, z) = Re + (Re_s - Re)\zeta(z, z_{-\infty}) \quad \text{if} \quad r \leqslant r_\infty \quad \text{and} \quad z < z_{-\infty}, \tag{2.6b}$$

$$\widetilde{Re} = \widetilde{Re}(r_\infty, z) + (Re_s - \widetilde{Re}(r_\infty, z))\zeta(r, r_\infty) \quad \text{if} \quad r > r_\infty\,, \tag{2.6c}$$

where ζ is the function defined by

$$\zeta(a, b) = \frac{1}{2} + \frac{1}{2}\tanh\left\{\alpha \tan\left(-\frac{\pi}{2} + \pi\frac{|a-b|}{l^s}\right)\right\}, \tag{2.7}$$

along with $\alpha = 4$. In addition to this artificial damping, numerical dissipation in the sponge zones is increased by progressive grid stretching. The governing equations are then solved using a uniform free-stream flow condition

$$\boldsymbol{u} = (0, 0, 1)^T, \ \varrho, \Theta = 1 \quad \text{on } \Gamma_{in} \cup \Gamma_{ext} \cup \Gamma_{out}. \tag{2.8}$$

We enforce additional no-slip adiabatic wall conditions at the body wall

$$\boldsymbol{u} = \boldsymbol{0}, \ \partial_n \Theta = 0 \quad \text{on } \Gamma_b, \tag{2.9}$$

where ∂/∂_n is the derivative normal to the surface.

We use the FreeFem++ software (http://www.freefem.org) to generate a two-dimensional triangulation of the azimuthal plane $\theta = 0$ with the Delaunay–Voronoi algorithm. The mesh refinement is controlled by the vertex densities imposed on both external and internal boundaries. Regions where the mesh density varies are depicted by the solid lines in figure 2. All equations are numerically solved by a finite-element method using the mesh M_1 shown in Appendix A to provide the most accurate results, built with $z_{-\infty} = -100$, $z_{\infty} = 300$, $r_{\infty} = 25$ and $l_s = 200$ and made of 662 816 triangles. A set of equations is first multiplied by r to avoid the singularity on the $r = 0$ axis. The associated variational formulation is then derived and spatially discretized onto a basis of Arnold–Brezzi–Fortin MINI elements (Matsumoto & Kawahara 2000), with four-node P_{1b} elements for the velocity components and three-node P_1 elements for the density and temperature. The sparse matrices resulting from the projection of these variational formulations onto the basis of finite elements are built with the FreeFem++ software.

3. Global stability analysis

The stability analysis relies on the existence of a steady solution about which perturbations are superimposed. The total flow field is split into a steady axisymmetric base flow $\boldsymbol{Q} = (\rho, U, 0, W, T, P)^T$ and a three-dimensional perturbation $\boldsymbol{q}' = (\rho', u', v', w', T', p')^T$ of small amplitude ϵ. Unless specified otherwise, we present here results pertaining only to the afterbody configuration, the results obtained for the sphere being very similar.

3.1. *Base flow calculations*

The base flow $\boldsymbol{Q}$ is solution of the steady axisymmetric form of the nonlinear system (2.4), written formally as

$$\mathscr{M}_0(\boldsymbol{Q}, \mathscr{G}) = \boldsymbol{0}, \tag{3.1}$$

where $\mathscr{M}_0$ is the axisymmetric form of operator $\mathscr{M}$. The base flow satisfies boundary conditions (2.8) and (2.9) along with the additional condition $U = 0$, $\partial_r W = \partial_r \rho = \partial_r T = 0$ on Γ_a obtained for axisymmetric solutions from mass, momentum and internal energy conservation as $r \to 0$. The base flow is obtained using an iterative Newton method (Barkley, Gomes & Henderson 2002): starting from a guess value $\bar{\boldsymbol{Q}}$, this method involves iterations of the guess value $\bar{\boldsymbol{Q}} + \delta\bar{\boldsymbol{Q}}$, where $\delta\bar{\boldsymbol{Q}}$ is the solution of a simple linear problem. At each step, a matrix inversion is performed using the UMFPACK library, which consists in a sparse direct LU solver (Davis & Duff 1997; Davis 2004). The process is carried out until the $\mathscr{L}^2$-norm of the residual of the governing equations for $\bar{\boldsymbol{Q}}$ becomes smaller than 10^{-12}. In the low-Mach-numbers limit, the flow quantities are expanded as power series in γM^2 (Nichols, Schmid & Riley 2007) and the initial guess is obtained by continuation from the incompressible solution computed using the solver presented in Meliga

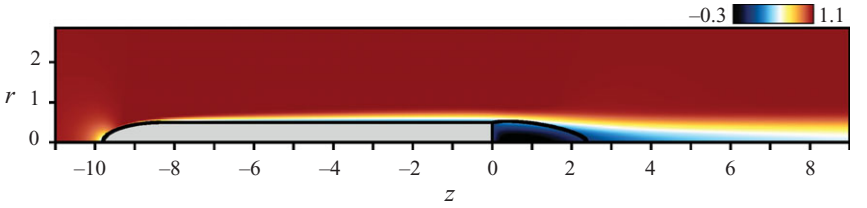

FIGURE 3. Afterbody flow: spatial distribution of the base flow streamwise velocity, $Re = 998.5$; $M = 0.5$.

et al. (2009*a*). For Mach numbers $M > 0.3$, the initial guess is simply chosen as a solution of the compressible equations computed for a lower value of the Mach number. Since we do not use the governing equations under their conservative form, the numerical method cannot easily account for the presence of shock waves in the computational domain, as this would require the use of mesh refinement techniques to fully resolve the viscous structure of the shock. Consequently, the local Mach number $M_l = M\|\boldsymbol{U}\|/\sqrt{T}$ must remain smaller than one everywhere in the flow, and the free-stream Mach number can therefore be increased up to $M \sim 0.7$ for the present computations.

The dynamics is from now on exemplified by setting $M = 0.5$. Figure 3 shows iso-contours of the base flow streamwise velocity W computed in the high subsonic regime ($Re = 998.5$, $M = 0.5$). The solid line is the streamline linking the separation point to the stagnation point on the $r = 0$ axis, and defines the separatrix delimiting the recirculation bubble developing in the lee of the afterbody, whose length is approximately 2.5 diameters. The negative values of the streamwise velocity close to the axis reach 30 % of the free-stream velocity.

3.2. *Eigenvalue calculations*

All perturbations are sought under the form of normal modes

$$\boldsymbol{q}' = \hat{\boldsymbol{q}}(r, z)\mathrm{e}^{(\sigma+\mathrm{i}\omega)t+\mathrm{i}m\theta} + \text{ c.c.}, \tag{3.2}$$

where $\hat{\boldsymbol{q}}$ is the eigenmode, the so-called global mode, for which both the cross-stream and streamwise directions are eigendirections. The azimuthal wavenumber of the global mode is m, its growth rate and pulsation are σ and ω, respectively. Substituting (3.2) into (2.4) and retaining only terms of order ϵ yields a system of equations governing the normal mode under the form of a generalized eigenvalue problem for $\lambda = \sigma + \mathrm{i}\omega$ and $\hat{\boldsymbol{q}}$:

$$\lambda\mathscr{B}(\boldsymbol{Q})\hat{\boldsymbol{q}} + \mathscr{A}_m(\boldsymbol{Q}, \mathscr{G})\hat{\boldsymbol{q}} = \boldsymbol{0}, \tag{3.3}$$

with $\mathscr{A}_m$ the complex linearized evolution operator obtained from $\mathscr{A} = \partial\mathscr{M}/\partial\boldsymbol{q}$ by replacing the θ derivatives by $\mathrm{i}m$, whose expression is detailed in Appendix D. The perturbation satisfies homogeneous boundary conditions linearized from the Navier–Stokes conditions, and the additional conditions at the axis Γ_a depend on the azimuthal wavenumber m. For the $m = \pm 1$ modes discussed throughout this study, we use the specific condition $\hat{w} = \hat{\rho} = \hat{T} = 0$, $\partial_r\hat{u} = \partial_r\hat{v} = 0$. This eigenproblem is solved using the 'implicitly restarted Arnoldi method' of the ARPACK library (http://www.caam.rice.edu/software/ARPACK) based upon a shift and invert strategy (Ehrenstein & Gallaire 2005).

To normalize the $m = \pm 1$ global modes, we impose first the phase of the radial velocity to be zero at $r = 0$ and $z = 1$, i.e. $\hat{u}(0, 1)$ is real positive. To normalize the

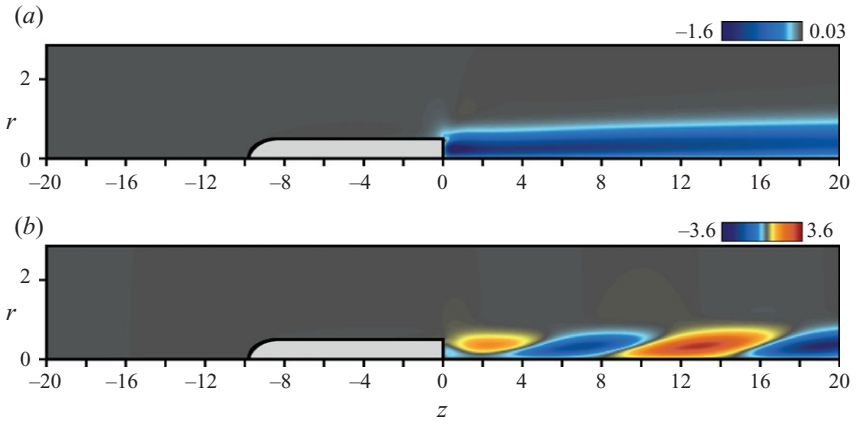

FIGURE 4. Afterbody flow: spatial distribution of streamwise velocity for the leading global modes, $M = 0.5$. The black hue corresponds to vanishing magnitudes of perturbation. (*a*) Stationary mode 1 at threshold of the first instability ($Re_1 = 483.5$). (*b*) Oscillating mode 2 at the threshold of the second instability ($Re_2 = 998.5$). Only the real part is shown.

mode amplitude, we introduce the near-wake domain Ω_{in} defined as

$$z \in [-12.3,\ 5.25\,] \quad \text{and} \quad r < 2 \qquad \text{(afterbody)}, \tag{3.4a}$$

$$z \in [-2.5,\ 5.25\,] \quad \text{and} \quad r < 2 \qquad \text{(sphere)}, \tag{3.4b}$$

shown as the dark grey shaded area in figure 2. We also use the inner product $\int_\Omega \hat{\boldsymbol{a}} \cdot \hat{\boldsymbol{b}}\, r \mathrm{d}\Omega$, where $\hat{\boldsymbol{a}}$ and $\hat{\boldsymbol{b}}$ belong to $\mathbb{C}^n$, $\mathrm{d}\Omega$ is the surface element on the computational domain Ω, and $\cdot$ refers to the canonical Hermitian scalar product in $\mathbb{C}^n$. The eigenmode is then normalized so that

$$\int_{\Omega_{in}} \hat{\boldsymbol{q}} \cdot \mathscr{B}\hat{\boldsymbol{q}}\, r \mathrm{d}\Omega = 1. \tag{3.5}$$

This normalization choice has no physical effect but eases the comparison between results obtained on different meshes when convergence tests are carried out. For incompressible flows, this choice has a simple physical interpretation, as the integrand reads simply

$$\hat{\boldsymbol{q}} \cdot \mathscr{B}\hat{\boldsymbol{q}} = \|\hat{\boldsymbol{u}}\|^2, \tag{3.6}$$

so that condition (3.5) imposes the kinematic energy of the perturbation to be unity in Ω_{in}. In the present compressible case, this inner product is convenient for the numerics but is not physically motivated, as the integrand does not represent any meaningful physical quantity, either the total energy or the total enthalpy of the perturbation. Still, we insist that the compressible effects discussed in the following are intrinsic and do not depend on the choice of the inner product.

For all values of the Mach number in the range $M < 0.7$ prevailing here, the sequence of bifurcations undergone by the axisymmetric solution is identical to that previously documented in the incompressible regime for spheres and disks (Natarajan & Acrivos 1993). When the Reynolds number is increased, the axisymmetric base flow is first destabilized at $Re_1(M)$ by a stationary mode 1 ($\omega = 0$) whose eigenvector chosen as $\hat{\boldsymbol{q}}_1 = (\hat{\rho}_1, \hat{u}_1, \mathrm{i}\hat{v}_1, \hat{w}_1, \hat{T}_1)^T$ is real using the present normalization. For the afterbody flow at $M = 0.5$, we find the critical Reynolds number $Re_1 = 483.5$ ($Re_1 = 212.5$ for

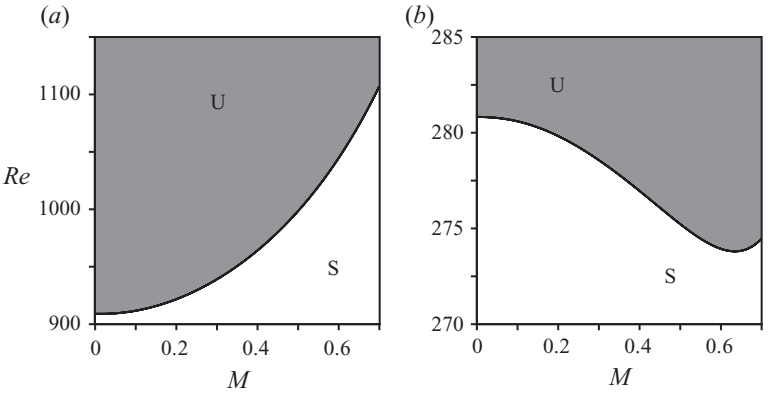

FIGURE 5. Oscillating mode 2: boundary separating the unstable domain (shaded area labelled U) from the stable domain (area labelled S) in the (M, Re) plane. (a) Afterbody. (b) Sphere.

the sphere at $M = 0.5$). Figure 4(a) shows the streamwise velocity disturbances $\hat{w}_1$ at threshold for the afterbody, which extend far downstream of the body. The velocity perturbation is negative in figure 4(a), meaning that the total flow slows down in this azimuthal plane. The azimuthal wavenumber of this mode being $m = 1$, the streamwise velocity perturbation is opposite on the other side of the revolution axis, where the total flow speeds up, hence inducing an off-axis displacement of the wake, as in the case of a sphere at zero Mach number (Johnson & Patel 1999). Owing to compressibility, similar effects exist for the temperature and density perturbations, although at a lower level of magnitude. Namely we find that the low-velocity wake region is hotter and lighter than the base flow, whereas the high-velocity wake region is cooler and heavier (not shown here for conciseness).

When the Reynolds number is increased further above Re_1, the axisymmetric solution is destabilized at the second threshold value $Re_2(M)$ by a pair of oscillating $m = 1$ modes of frequency $\omega = \pm\omega_2$, whose eigenvectors are complex conjugates. In the following, only the mode of frequency ω_2, named mode 2, will be discussed, its eigenvector being denoted $\hat{\boldsymbol{q}}_{\boldsymbol{2}} = (\hat{\rho}_2, \hat{u}_2, \mathrm{i}\hat{v}_2, \hat{w}_2, \hat{T}_2)^T$. For the afterbody flow at $M = 0.5$, we find a critical Reynolds number $Re_2 = 998.5$ and a frequency $\omega_2 = 0.40$ corresponding to a Strouhal number $St = \omega_2 D/(2\pi U_\infty) = 0.063$ (resp. $Re_2 = 275.2$, $\omega_2 = 0.66$ and $St = 0.11$ for the sphere at $M = 0.5$). Figure 4(b) shows the real parts of the streamwise velocity disturbances $\hat{w}_{2r}$ at threshold for the afterbody: it exhibits positive and negative velocity perturbations alternating downstream of the body, in a regular, periodic way that defines a spatial period of approximately 12 diameters. The imaginary part (not shown here) displays a similar structure, but are approximately in spatial quadrature with extrema located close to the nodes of the real parts. This mode therefore corresponds to the development of a spiral in the wake of the body, which rotates in time at the frequency ω_2.

3.3. *Impact of compressibility*

We investigate from now on the effect of the free-stream Mach number on the flow stability by focusing on the oscillating mode 2, which is expected to dominate the flow dynamics at sufficiently large Reynolds numbers. The subscript 2 is therefore systematically omitted to ease the notation.

We show in figure 5(a) the boundary of the stability domain for mode 2 in the (M, Re) plane: the flow is unstable (resp. stable) for combinations of parameters

located in the shaded region labelled U (resp. in the white region labelled S). The values for $M=0$ arise from the resolution of the incompressible stability problem on a mesh made only of the inner cylinder defined by (2.5*a*), the numerical method being derived from Meliga *et al.* (2009*a*) and Meliga, Chomaz & Sipp (2009*b*). Owing to the choice of the reference scales, the low-Mach-number limit agrees with the incompressible results without supplemental rescaling. Compressibility has a stabilizing effect as increasing the Mach number is seen to yield a moderate increase in the critical Reynolds number, by approximately 17 % (from $Re_2=909.1$ at $M=0$ to 1061.1 at $M=0.7$). Still, it must not be inferred from the present study that compressibility systematically acts as a stabilizing mechanism for compressible wake flows. Indeed, we present in figure 5(*b*) the boundary of the stability domain for the sphere: interestingly, increasing the Mach number from small values now yields a destabilizing effect, as the critical Reynolds number decreases by approximately 3 % (from $Re_2=280.8$ at $M=0$ to 273.8 at $M\simeq 0.63$). In contrast, the stabilizing effect already documented for the afterbody flow is ultimately retrieved for high subsonic Mach numbers. Although such variations may seem small, it will be shown in the following section that they are the consequence of competitive significant effects that are simultaneously at work.

3.4. *Effect of the baroclinic torque*

It has been suggested by Soteriou & Ghoniem (1995) that the difference in the stability properties of homogeneous and non-homogeneous shear layers results from the existence of a baroclinic torque. The main idea is that a baroclinic torque arising from misaligned gradients of base flow density and pressure perturbations, reading

$$\boldsymbol{\Gamma}=\frac{1}{\gamma M^2}\boldsymbol{\nabla}\hat{p}\times\boldsymbol{\nabla}\left(\frac{1}{\rho}\right), \tag{3.7}$$

can act as a source term for the vorticity perturbations. For the parameter setting prevailing here, the existence of this torque has been used in a previous paper by the authors to interpret the stabilizing effect of compressibility observed for model parallel wakes (Meliga, Sipp & Chomaz 2008). The main idea, originally formulated by Nichols *et al.* (2007), is that the baroclinic torque, which arises from the shear layer undulation, induces a further deformation which is out of phase with the total shear layer displacement, thus decreasing the temporal growth of the absolutely unstable mode.

To assess the effect of the baroclinic torque on the global stability of the fully non-parallel wake flows considered here, we generalize the idea initially introduced by Lesshafft & Huerre (2007) in the context of parallel hot jets. These authors proposed solving a modified dispersion relation in which the linearized momentum equations are artificially forced so as to cancel the baroclinic torque. In this case, the torque has only one non-trivial component owing to the parallel assumption and to the axisymmetry of the relevant disturbances. In contrast, the torque is fully three-dimensional here, owing to the non-parallelism of the flow and to the non-axisymmetry of the relevant disturbances. In practice, we solve the forced compressible stability problem

$$(\lambda+\delta_{\boldsymbol{\Gamma}}\lambda)\mathscr{B}(\boldsymbol{Q})\hat{\boldsymbol{q}}+\mathscr{A}_m(\boldsymbol{Q},\mathscr{G})\hat{\boldsymbol{q}}=\rho\boldsymbol{S}\hat{\boldsymbol{q}}, \tag{3.8}$$

where $\delta_{\boldsymbol{\Gamma}}\lambda$ is the eigenvalue variation resulting from the addition of the forcing term $\boldsymbol{S}$, appropriately defined by

$$\boldsymbol{S}\hat{\boldsymbol{q}}=-\frac{1}{\gamma M^2}\hat{p}\,\boldsymbol{\nabla}\left(\frac{1}{\rho}\right). \tag{3.9}$$

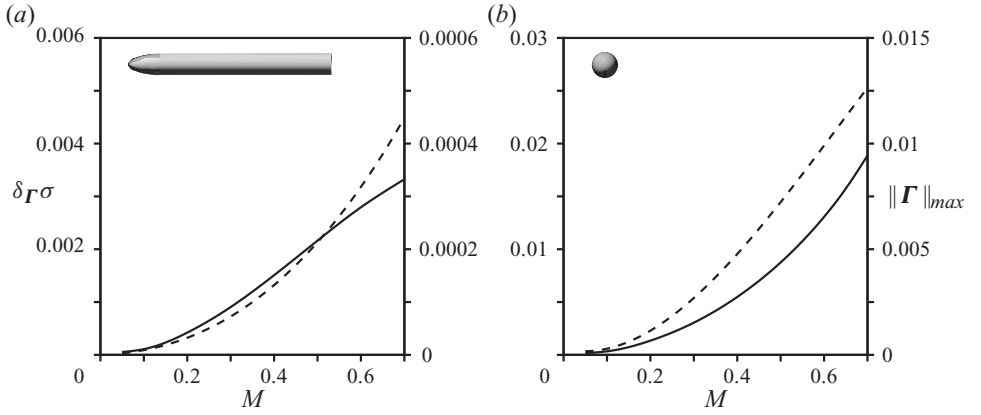

FIGURE 6. Effect of the baroclinic torque on the oscillating mode 2 at the threshold of instability, i.e. for parameter settings along the neutral curve shown in figure 5. (*a*) Afterbody. (*b*) Sphere. The solid curve stands for the growth rate variation $\delta_{\boldsymbol{\Gamma}}\sigma$ induced by an appropriate forcing defined by (3.9), whose aim is to cancel the effect of the baroclinic torque. The dashed curve represents the maximum magnitude of the baroclinic torque.

It can be checked that $\nabla\times(\boldsymbol{S}\hat{\boldsymbol{q}})=-\boldsymbol{\Gamma}$, meaning that this forcing exactly counterbalances the baroclinic term when one recasts the momentum equations into their vorticity counterpart. When considering the growth rate variation $\delta_{\boldsymbol{\Gamma}}\sigma$, a positive value means that cancelling the baroclinic torque has a destabilizing effect, i.e. the baroclinic effects are stabilizing. On the contrary, a negative value means that cancelling the baroclinic torque has a stabilizing effect, i.e. that baroclinic effects are destabilizing.

The solid lines in figures 6(*a*) and 6(*b*) represent the variation $\delta_{\boldsymbol{\Gamma}}\lambda$ computed along the neutral curves shown in figure 5. For both configurations, we find positive variations, meaning that the torque has a stabilizing effect, a result consistent with the results arising from the local analysis. Moreover, this effect increases with the Mach number, as both curves are monotonically increasing. This is due to the increasing magnitude of the torque, as depicted by the dashed lines in figure 6, which present the maximum amplitude of the baroclinic torque $\|\boldsymbol{\Gamma}\|_{max}$ as a function of the Mach number. Still, such results question the usual interpretation of compressibility in terms of baroclinic effects, as the effect of the torque is identical for both the afterbody and the sphere, the difference being only in order of magnitude. In particular, this approach does not explain the destabilizing effect observed in the case of the sphere.

4. Sensitivity analysis to a modification of the Mach number

We investigate how the stability of the global mode, taken at threshold of instability, is affected by a small but finite modification of the Mach number of magnitude δM. A given eigenvalue λ is explicitly a function of the base flow $\boldsymbol{Q}$ and of the Mach number. The base flow itself being an implicit function of the Mach number, the eigenvalue can be written formally as $\lambda=\lambda(\boldsymbol{Q}(M), M)$. To understand the complex compressible effects discussed in § 3.3, one must therefore keep in mind that when the Mach number varies from M to $M+\delta M$, compressible effects are simultaneously at work at two different levels: (i) at the perturbation level, as a result of the change in the Mach number in the disturbance equations, (ii) at the base flow level, as a result of the change in the Mach number in the base flow equations. From this point of view,

the baroclinic torque defined in (3.7) can be written formally as $\boldsymbol{\Gamma} = \boldsymbol{\Gamma}(\boldsymbol{Q}(M), M)$, meaning that the introduction of the forcing term (3.9) acts both at the disturbance and the base flow levels.

The effect at the disturbance level corresponds to a fictitious flow for which the base flow would be artificially frozen. Actually, it corresponds to the effect investigated up to now in the framework of the local stability of parallel flows. Indeed, in this approach, the base flow is not a solution of the governing equations. It is prescribed under the form of analytical profiles independent of the Mach number and satisfying the inviscid equations: see, for instance, the model velocity profiles introduced by Monkewitz & Sohn (1988) to study the stability of hot jets, and recently used to assess the effect of compressibility on the stability of jets and wakes (Lesshafft & Huerre 2007; Meliga *et al.* 2008). In contrast, the effect at the base flow level corresponds to a fictitious flow for which the Mach number would remain constant in the disturbance equations whereas the base flow would adapt the variations of compressibility, an effect which lies outside the scope of most local analyses, for which a compressible Mach squared correction can be included only in the base density and temperature profiles by adding in the Crocco–Busemann relation to the governing equations (Pavithran & Redekopp 1989; Jackson & Grosch 1990). Although such an approach has proved fruitful in providing quantitative results for weakly non-parallel shear flows such as mixing layers and jets, it will be shown here that the change in the base momentum profiles is exactly the key to interpretation of the stability of compressible, non-parallel wake flows.

Provided the Mach number modification is small enough for the linear assumption to hold, it is possible to analyse separately both effects, which are in the end likely to affect the disturbance dynamics. The eigenvalue variation induced by a change in the Mach number δM can therefore be written as

$$\delta\lambda = \frac{\partial\lambda}{\partial M}\delta M + \frac{\partial\lambda}{\partial \boldsymbol{Q}}\frac{\partial \boldsymbol{Q}}{\partial M}\delta M = \delta_M\lambda + \delta_{\boldsymbol{Q}}\lambda, \tag{4.1}$$

with $\delta_M\lambda$ the variation induced at the perturbation level, and $\delta_{\boldsymbol{Q}}\lambda$ the variation induced by the implicit modification of the base flow. The expression of each specific variation can be derived by carrying out direct stability calculations, as developed in Appendix B. However, such an approach is extremely computationally intensive and time-consuming owing to the tremendous number of degrees of freedom involved. We rather use here a more systematic technique relying on sensitivity analyses, whose aim is to compute the gradients of the eigenvalue with respect to the Mach number and to the base flow variables. This analysis relies on the computation of an adjoint global mode $\hat{\boldsymbol{q}}^\dagger = (\hat{\rho}^\dagger, \hat{\boldsymbol{u}}^\dagger, \hat{T}^\dagger, \hat{p}^\dagger)^T$, i.e. a Lagrange multiplier for the global mode, obtained as the solution of an eigenvalue problem. Such an approach is classically used in flow control and optimization problems (Luchini & Bottaro 1998; Gunzburger 1999; Corbett & Bottaro 2000, 2001). The detailed calculations are postponed to Appendix C, and we only mention here that the adjoint global mode is normalized with respect to the global mode so that

$$\int_\Omega \hat{\boldsymbol{q}}^\dagger \cdot \mathscr{B}\hat{\boldsymbol{q}}\, r \,\mathrm{d}\Omega = 1. \tag{4.2}$$

The specific localization of the adjoint global modes resulting from the convective non-normality of the linearized evolution operator (Chomaz 2005; Marquet *et al.* 2009) is illustrated for the afterbody flow in figure 7, where one observes high amplitudes within the recirculating bubble and steadily decreasing amplitudes upstream of the

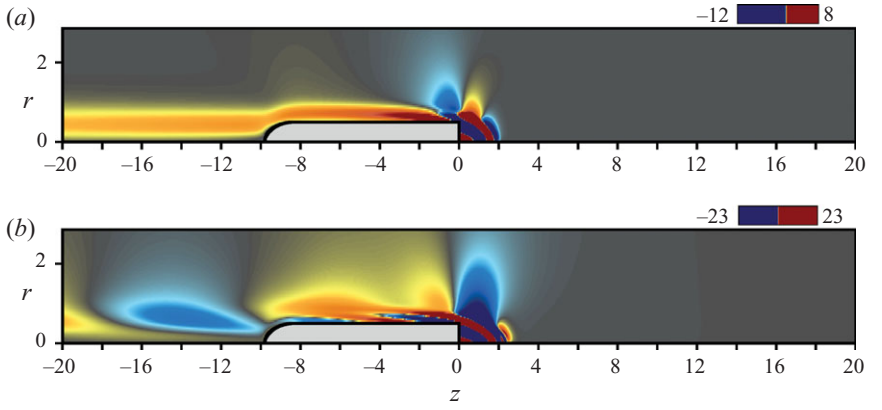

FIGURE 7. Same as figure 4 for the oscillating adjoint global modes at threshold of instability.

body, as classically reported for incompressible wakes (Meliga *et al.* 2009*b*). The correctness and accuracy of the adjoint method is assessed in Appendix B, where we present a comparison between the values of the variations $\delta\sigma/\delta M$ arising from the adjoint formalism and that arising from direct stability calculations.

4.1. *Compressible effects at the disturbance level*

A change of the Mach number in the disturbance equations induces a change in the pressure gradient exerted on the perturbation and in the amount of energy it exchanges with the base flow. In practice, when the Mach number is increased from M to $M+\delta M$, the flow stability is altered as a forcing term $\boldsymbol{\delta\hat{f}}$ proportional to the perturbation quantities occurs in the right-hand side of the disturbance equations:

$$\boldsymbol{\delta\hat{f}} = \left(0,\ \frac{2}{\gamma M^3}\nabla\hat{p},\ 2\gamma(\gamma-1)\frac{M}{Re}\left(\boldsymbol{\tau}(\boldsymbol{U}):\boldsymbol{d}(\hat{\boldsymbol{u}})+\boldsymbol{\tau}(\hat{\boldsymbol{u}}):\boldsymbol{d}(\hat{\boldsymbol{u}})\right)\right)^T \delta M. \tag{4.3}$$

The resulting eigenvalue variation $\delta_M\lambda$ is computed here assuming that the base flow is artificially kept constant. If δM is small, the forcing (4.3) acts as a weak perturbation of the linearized evolution operator under the form of momentum and internal energy sources in the perturbation equations (Giannetti & Luchini 2003, 2007). Following these authors, the variation is simply given by projection of the forcing onto the adjoint global mode:

$$\delta_M\lambda = \int_\Omega \hat{\boldsymbol{q}}^\dagger\cdot\boldsymbol{\delta\hat{f}}\, r\,\mathrm{d}\Omega, \tag{4.4}$$

the corresponding growth rate variation being obtained by retaining only the real part of (4.4).

4.2. *Compressible effects at the base flow level*

A change to the Mach number in the base flow equations induces a change in the pressure gradient exerted on the base flow and in the viscous dissipation of its energy. In practice, the flow stability is altered, as the base flow on which disturbances develop is modified. Provided δM is small, the base flow solution of (3.1) for the new Mach number $M+\delta M$ can indeed be approximated by $\boldsymbol{Q}+\boldsymbol{\delta Q}$, where $\boldsymbol{\delta Q}$ is the base flow

modification computed as the solution of the linear problem

$$\mathscr{A}_0(\boldsymbol{Q}, M)\delta\boldsymbol{Q} = \left(0,\ \frac{2}{\gamma M^3}\nabla P\ ,\ 2\gamma(\gamma-1)\frac{M}{Re}\,\boldsymbol{\tau}(\boldsymbol{U}):\boldsymbol{d}(\boldsymbol{U})\right)^T \delta M. \tag{4.5}$$

The resulting variation $\delta_{\boldsymbol{Q}}\lambda$ is computed here assuming that the Mach number remains constant in the disturbance equations. To this end, we generalize now to compressible flows the sensitivity analysis to base flow modifications, as originally formulated for parallel flows by Bottaro *et al.* (2003) and Hwang & Choi (2006) and recently generalized to spatially developing flows by Marquet *et al.* (2008), whose aim is to compute the gradients of the eigenvalue with respect to the base flow variables. All results are from now on discussed in terms of the physically relevant conservative variables, as the modification of base flow density also integrates effects of the modification of momentum and internal energy when using non-conservative variables. To this end, the base flow is recast into conservative variables, namely $\boldsymbol{Q}_{\boldsymbol{c}} = (\rho, \rho\boldsymbol{U}, \rho T, P)^T$. The corresponding base flow modification can be simply expressed in terms of $\delta\boldsymbol{Q}$ as

$$\delta\boldsymbol{Q}_{\boldsymbol{c}} = \mathscr{H}\delta\boldsymbol{Q}, \tag{4.6}$$

with $\mathscr{H}$ the matrix mapping from non-conservative onto conservative perturbation quantities. Introducing the complex fields $\nabla_\rho\lambda$, $\nabla_{\rho U}\lambda$, $\nabla_{\rho T}\lambda$ and $\nabla_P\lambda$ defining the sensitivity of the eigenvalue to a modification of the base flow density, momentum, internal energy and pressure, the eigenvalue variation can be written as

$$\delta_{\boldsymbol{Q}}\lambda = \int_\Omega \left(\nabla_\rho\lambda\cdot\delta\rho + \nabla_{\rho U}\lambda\cdot\delta(\rho\boldsymbol{U}) + \nabla_{\rho T}\lambda\cdot\delta(\rho T) + \nabla_P\lambda\cdot\delta P\right) r\,\mathrm{d}\Omega, \tag{4.7}$$

the corresponding sensitivities for the growth rate being obtained by retaining only the real parts of these complex fields. The sensitivity of the eigenvalue to base flow modifications is defined by the field $\nabla_{\boldsymbol{Q}_c}\lambda = (\nabla_\rho\lambda, \nabla_{\rho U}\lambda, \nabla_{\rho T}\lambda, \nabla_P\lambda)^T$, so that

$$\delta_{\boldsymbol{Q}}\lambda = \int_\Omega \nabla_{\boldsymbol{Q}_c}\lambda\cdot\delta\boldsymbol{Q}_{\boldsymbol{c}}\, r\,\mathrm{d}\Omega. \tag{4.8}$$

Using the normalization condition (4.2), we obtain

$$\nabla_{\boldsymbol{Q}_c}\lambda = -\mathscr{H}^\dagger\left\{\frac{\partial}{\partial\boldsymbol{Q}}\left(\lambda\mathscr{B}\hat{\boldsymbol{q}} + \mathscr{A}_m\hat{\boldsymbol{q}}\right)\right\}^\dagger \hat{\boldsymbol{q}}^\dagger, \tag{4.9}$$

where the † superscript denotes the adjoint of the preceding operator (see Appendix C).

4.3. *Application to the observed compressible effects*

For both configurations, we have computed the variations $\delta_{\boldsymbol{Q}}\sigma/\delta M$ and $\delta_M\sigma/\delta M$ along the neutral curve of the oscillating modes 2 presented in figure 5. Results are shown as the dashed and dash-dotted lines in figure 8, where the overall variation $\delta\sigma/\delta M$ computed from (4.1) is also reported as the solid line. Positive values (resp. negative values) mean that an increase in the Mach number induces an increase (resp. decrease) in the growth rate, and therefore correspond to a destabilizing (resp. stabilizing) effect. The variation $\delta_M\sigma/\delta M$ is negative for both configurations, meaning that the compressible effects at the disturbance level are always stabilizing. This result is consistent with the idea arising from local analyses that an increase in the Mach number prevents the upstream propagation of disturbance waves and thus yields a stabilization of shear flows by promoting a convective instability

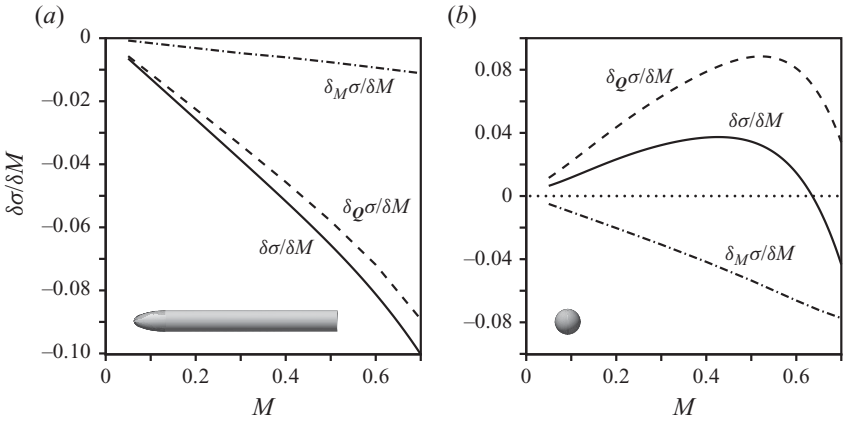

FIGURE 8. Variation $\delta\sigma/\delta M$ corresponding to a small modification of the Mach number, computed along the neutral curves shown in figure 5 for the oscillating mode 2 at the threshold of instability. (*a*) Afterbody. (*b*) Sphere. The solid curve stands for the overall variation $\delta\sigma/\delta M$. The dashed and dash-dotted curves represent the variations $\delta_{\boldsymbol{Q}}\sigma/\delta M$ and $\delta_M\sigma/\delta M$ corresponding respectively to the base flow variation $\partial\boldsymbol{Q}/\partial M$, and to the modification of the Mach number in the disturbance equations.

(Pavithran & Redekopp 1989). In contrast, the compressible effects at the base flow level are stabilizing for the afterbody ($\delta_{\boldsymbol{Q}}\sigma/\delta M \leqslant 0$) but destabilizing for the sphere ($\delta_{\boldsymbol{Q}}\sigma/\delta M \geqslant 0$). The key idea here is thus that the compressible effects discussed in § 3.3 are triggered by the modification of the base flow profiles on which disturbances develop. For the afterbody, the overall stabilizing effect of compressibility is indeed due to the domination of the variation $\delta_{\boldsymbol{Q}}\sigma/\delta M$, which represents 90 % of the total variation in the range of Mach numbers considered. Both contributions are significant for the sphere, hence explaining the small variations of the Reynolds numbers mentioned previously on this configuration. Still, the overall destabilizing effect again results from the variation $\delta_{\boldsymbol{Q}}\sigma/\delta M$ being dominant for $M \leqslant 0.63$ (this limit value being in excellent agreement with the one above which the effect of compressibility is reversed and starts being stabilizing, as seen from figure 5*b*).

5. Physical interpretation

5.1. *Effect of the advection and production mechanisms*

For a base flow modification $\boldsymbol{\delta Q}$, it is possible to interpret the eigenvalue variation in terms of a competition between an advection mechanism and a production mechanism. In the local theory, this distinction has been formalized via the concepts of convective and absolute instability: the flow is said to be locally convectively unstable if the advection of disturbances by the base flow dominates over their production, and locally absolutely unstable when production is strong enough to sustain the flush of the base flow. For incompressible flows, Marquet *et al.* (2008) have shown that it is straightforward to split the sensitivity function and to identify contributions accounting for the advection and production of disturbances. The case of compressible flows is more involved, as the perturbation may exchange energy with the base flow in different ways. To identify advection and production terms, we linearize the governing equations, first expressed using an integral formulation and conservative

variables. The physical origin of all terms in (3.3) then naturally arises when turning back into non-conservative variables. For instance, the nonlinear term $\varrho \boldsymbol{u}\cdot\boldsymbol{\nabla u}$ in the momentum equation (2.1*b*) corresponds to the advection of momentum by the flow. Its linearization gives rise to two classes of terms in the linearized momentum equation: (*a*) $\hat{\rho}\boldsymbol{U}\cdot\boldsymbol{\nabla U}+\rho\boldsymbol{U}\cdot\boldsymbol{\nabla}\hat{\boldsymbol{u}}$ is an advection term corresponding to the advection of the momentum disturbance $\hat{\rho}\boldsymbol{U}+\rho\hat{\boldsymbol{u}}$ by the base flow, (*b*) $\rho\hat{\boldsymbol{u}}\cdot\boldsymbol{\nabla U}$ is a production term corresponding to the reciprocal advection of the base flow momentum $\rho\boldsymbol{U}$ by the perturbation. It is thus possible to gather all advection terms into the single advection operator $\mathscr{C}_m$ accounting for the advection of the perturbation (see Appendix D for a detailed expression). All other terms are production terms accounting for the production of disturbances through the advection of the base flow quantities by the perturbation and through the sink/source terms of the governing equations.

It is now possible to split the eigenvalue variation into $\delta_{\boldsymbol{Q}}\lambda=\delta_{\boldsymbol{Q},A}\lambda+\delta_{\boldsymbol{Q},P}\lambda$, where $\delta_{\boldsymbol{Q},A}\lambda$ is the variation arising from the change in the advection terms and $\delta_{\boldsymbol{Q},P}\lambda$ is the variation arising from the change in the production terms. Physically, a positive value of $\delta_{\boldsymbol{Q},A}\lambda$ indicates a destabilization of the eigenmode owing to a weakening of the disturbances advection. Similarly, a positive value of $\delta_{\boldsymbol{Q},P}\lambda$ indicates a destabilization owing to an increase in the production of disturbances. These terms are computed respectively as

$$\delta_{\boldsymbol{Q},A}\lambda=\int_{\Omega}\boldsymbol{\nabla}_{\boldsymbol{Q}_c,A}\lambda\cdot\boldsymbol{\delta Q_c}\,r\,\mathrm{d}\Omega,\quad \delta_{\boldsymbol{Q},P}\lambda=\int_{\Omega}\boldsymbol{\nabla}_{\boldsymbol{Q}_c,P}\lambda\cdot\boldsymbol{\delta Q_c}\,r\,\mathrm{d}\Omega, \tag{5.1}$$

where $\boldsymbol{\nabla}_{\boldsymbol{Q}_c,A}\lambda$ and $\boldsymbol{\nabla}_{\boldsymbol{Q}_c,P}\lambda$ are the advection and production sensitivity functions, computed by isolating the contribution of the advection and production terms in the sensitivity functions (4.9). We obtain simply

$$\boldsymbol{\nabla}_{\boldsymbol{Q}_c,A}\lambda=-\mathscr{H}^{\dagger}\left\{\frac{\partial}{\partial\boldsymbol{Q}}\left(\lambda\mathscr{B}\hat{\boldsymbol{q}}+\mathscr{C}_m\hat{\boldsymbol{q}}\right)\right\}^{\dagger}\hat{\boldsymbol{q}}^{\dagger},\quad \boldsymbol{\nabla}_{\boldsymbol{Q}_c,P}\lambda=\boldsymbol{\nabla}_{\boldsymbol{Q}_c}\lambda-\boldsymbol{\nabla}_{\boldsymbol{Q}_c,A}\lambda. \tag{5.2}$$

Figure 9(*a*) presents the values of $\delta_{\boldsymbol{Q},A}\sigma/\delta M$ (solid line) and $\delta_{\boldsymbol{Q},P}\sigma/\delta M$ (dash-dotted line) computed from (5.1) as functions of the Mach number, at the critical Reynolds number. The total variation $\delta_{\boldsymbol{Q}}\sigma/\delta M$ shown in figure 8 is also reported as the dashed line. The contribution of the production terms is negative, meaning that increasing the Mach number is stabilizing by weakening the production of disturbances for both the afterbody and the sphere. This contrasts with the contribution of the advection terms, which is found to be strikingly different: it is negative for the afterbody, for which the downstream advection of disturbances is strengthened and thus yields a simultaneously stabilizing effect when the Mach number increases; however, it is positive for the sphere, for which the downstream advection strongly weakens and yields a competitive destabilizing effect. For both the afterbody and the sphere, the effect of advection dominates over that of production. When the Mach number is varied, the change in the advection of disturbances resulting from the modification of the base flow profiles is therefore the leading mechanism, hence explaining why the compressible effects discussed in § 3.3 differ for both configurations.

As an attempt to further analyse this mechanism, we have computed separately the contribution of the four components of the state vector to the variation $\delta_{\boldsymbol{Q},A}\sigma$,

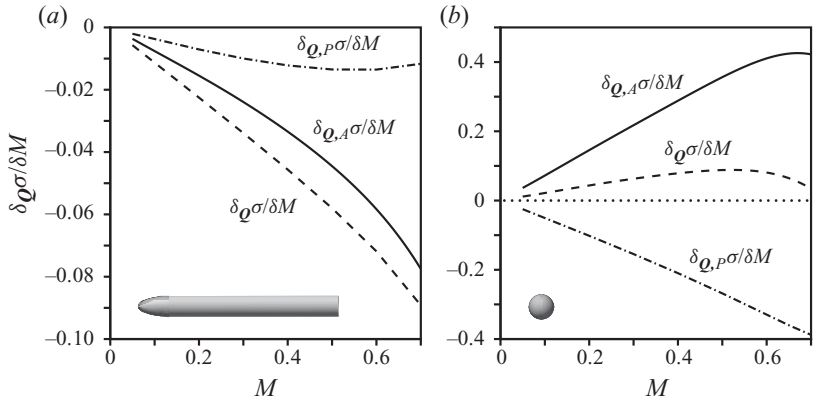

FIGURE 9. Growth rate variation corresponding to a small modification of the Mach number, computed for the oscillating mode 2 at the threshold of instability. (*a*) Afterbody. (*b*) Sphere. The dashed line represents the variation $\delta_{\boldsymbol{Q}}\sigma/\delta M$. The solid line (resp. dash-dotted line) represents the contribution of the variation $\delta_{\boldsymbol{Q},A}\sigma/\delta M$ owing to the modification of the advection mechanism (resp. the variation $\delta_{\boldsymbol{Q},P}\sigma/\delta M$ owing to the modification of the production mechanism), so that $\delta_{\boldsymbol{Q}}\sigma/\delta M$ is the sum of these two contributions.

defined as

$$\left.\begin{aligned} \delta_{\rho,A}\lambda &= \int_\Omega \nabla_{\rho,A}\lambda\cdot\delta\rho\, r\,\mathrm{d}\Omega, & \delta_{\rho\boldsymbol{U},A}\lambda &= \int_\Omega \nabla_{\rho\boldsymbol{U},A}\lambda\cdot\boldsymbol{\delta}(\rho\boldsymbol{U})\, r\,\mathrm{d}\Omega,\\ \delta_{\rho T,A}\lambda &= \int_\Omega \nabla_{\rho T,A}\lambda\cdot\delta(\rho T)\, r\,\mathrm{d}\Omega, & \delta_{P,A}\lambda &= \int_\Omega \nabla_{P,A}\lambda\cdot\delta P\, r\,\mathrm{d}\Omega, \end{aligned}\right\} \tag{5.3}$$

so that $\delta_{\boldsymbol{Q},A}\lambda$ is the sum of these four contributions. Physically, $\delta_{\rho\boldsymbol{U},A}\sigma$ corresponds to the growth rate variation induced by the modification of the base flow momentum in the terms already identified as advection terms, i.e. the variation that would be computed in a fictitious flow for which only the momentum components would be allowed to vary, all other components being kept artificially fixed. Of course, for real developing flows such as those considered here, the Mach number acts by modifying all components of the base flow, meaning that the modifications of density, momentum, internal energy and pressure cannot be prescribed individually but are connected to one another through relation (4.5). Such a decomposition is therefore qualitative and is used only as a means to gain insight at the mechanisms at work by estimating the importance of each individual base flow component in the complex effect observed.

Results of decomposition (5.3) are given in table 1, where the dominant contribution is systematically displayed in a grey shaded cell, so as to ease the reading. We find that when the Mach number is varied, the induced growth rate variation is entirely dominated by the contribution of momentum, as the density, energy and pressure modifications contribute very little to the overall variations. Such results have important physical interpretations in terms of base flow calculations, as they suggest that small errors in the computation of ρ and T have a limited impact on the stability of the oscillating mode 2. They also indicate that the compressible correction of the base density and temperature profiles that can be included in the local approach by use of the Crocco–Busemann relation is not relevant to the case

	Total	$\delta\rho$	$\boldsymbol{\delta(\rho U)}$	$\delta(\rho T)$	δP
Afterbody	-4.4×10^{-2}	2.4×10^{-4}	-4.5×10^{-2}	-6.4×10^{-7}	0
Sphere	3.6×10^{-1}	-2.3×10^{-3}	3.6×10^{-1}	-7.3×10^{-4}	0

TABLE 1. Oscillating mode 2 at the threshold of instability, $M=0.5$: growth rate variation $\delta_{\boldsymbol{Q},A}\sigma/\delta M$ induced by the modification of the advection mechanism. The variations $\delta_{\rho,A}\sigma/\delta M$, $\delta_{\rho\boldsymbol{U},A}\sigma/\delta M$, $\delta_{\rho T,A}\sigma/\delta M$ and $\delta_{P,A}\sigma/\delta M$ are obtained by evaluating the individual variations arising from the modification of density, momentum, internal energy and pressure, so that the overall variation $\delta_{\boldsymbol{Q},A}\sigma/\delta M$ is the sum of these four contributions.

	Total	$\boldsymbol{\delta(\rho U)_\perp}$	$\boldsymbol{\delta(\rho U)_\parallel}$
Afterbody	-4.5×10^{-2}	-8.1×10^{-2}	3.7×10^{-2}
Sphere	3.6×10^{-1}	-1.0×10^{-1}	4.6×10^{-1}

TABLE 2. Oscillating mode 2 at the threshold of instability, $M=0.5$: growth rate variation $\delta\sigma/\delta M$ induced by the modification of the cross-stream and streamwise momentum components.

of wake flows, for which the correct compressible effects are entirely triggered by the momentum components.

The dominant variation $\delta_{\rho\boldsymbol{U},A}\sigma/\delta M$ can itself be split into its contributions related to cross-stream and streamwise momentum, as reported in table 2 using the subscripts $\perp$ and $\parallel$, respectively. For both the afterbody and the sphere, the modification of the cross-stream momentum component is stabilizing, whereas that of the streamwise component is destabilizing. Still, if cross-stream momentum induces variations of same order of magnitude in both cases, the streamwise component induces a variation larger by one order of magnitude for the sphere. This competition between cross-stream and streamwise advection precisely explains the opposite compressible effects reported for the two geometries. The afterbody flow is indeed stabilized because the modification of the cross-stream advection of disturbances is dominant, whereas the sphere flow is destabilized since the modification of the streamwise advection dominates.

5.2. *Discussion*

Regions in space responsible for the destabilizing weakening of the advection mechanism triggered by the streamwise momentum component may be identified by plotting the spatial distribution of the integrand $\nabla_{\rho\boldsymbol{U}\parallel,A}\sigma\cdot\partial(\rho W)/\partial M$ (figures 10*a* and 10*b*), whose integration over space yields the variation $\delta_{\rho\boldsymbol{U}\parallel,A}\sigma/\delta M$. The colour look-up table has been set up so that the dark grey hue indicates vanishing contributions, hence showing that the magnitude is almost zero everywhere in the flow, except in the core of the recirculating bubble. The latter region exhibits a complex alternation of regions contributing either to a stabilization (negative values) or to a destabilization (positive values) of the flow. The difference between the afterbody and the sphere is limited to the magnitude of the integrand, which is about 2–3 times larger for the sphere, and to the existence of a strongly stabilizing region located very close to the afterbody base.

This difference does not arise from a different level of sensitivity, as the spatial distributions of the gradient $\nabla_{\rho\boldsymbol{U}\parallel,A}\sigma$ presented in figures 10(*c*) and 10(*d*) are remarkably similar, but from the base flow modification itself. We present in figures 10(*e*) and 10(*f*) the spatial distribution of the modification of streamwise

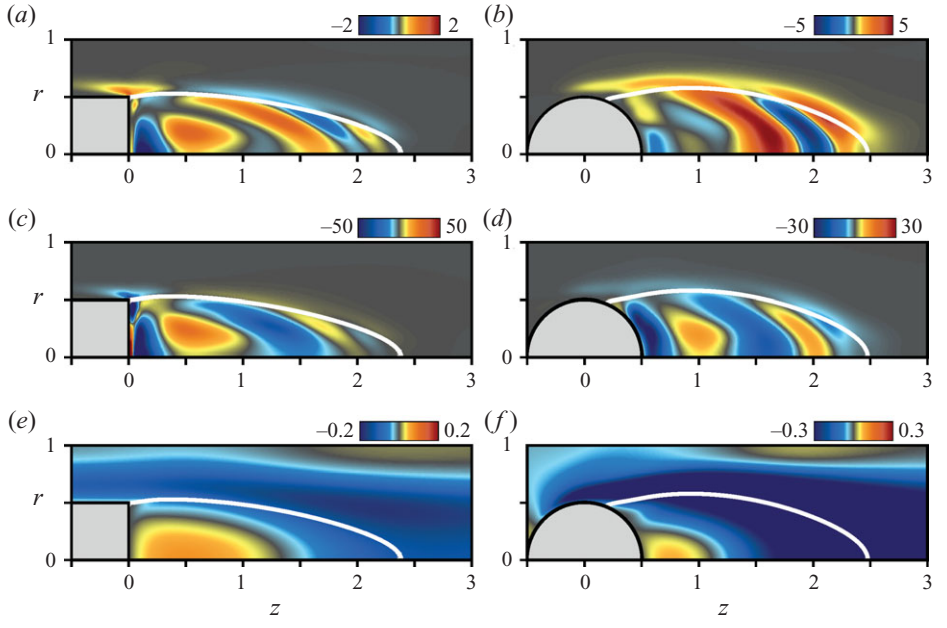

FIGURE 10. Oscillating mode 2 at the threshold of instability, $M = 0.5$. (*a*) Spatial distribution of the momentum integrand $\nabla_{\rho \boldsymbol{U}\parallel,A}\sigma \cdot \partial(\rho W)/\partial M$ for the afterbody. The integration over space of this flow field yields the variation $\delta_{\rho \boldsymbol{U}\parallel,A}\sigma/\delta M$ involved in the stabilizing/destabilizing effect of compressibility. The grey hue corresponds to vanishing magnitudes of the integrand. (*b*) Same as (*a*) for the sphere. (*c*) Spatial distribution of the gradient $\nabla_{\rho \boldsymbol{U}\parallel,A}\sigma$ for the afterbody. (*d*) Same as (*c*) for the sphere. (*e*) Spatial distribution of the streamwise momentum variation $\partial(\rho W)/\partial M$ for the afterbody. (*f*) Same as (*e*) for the sphere.

momentum $\partial(\rho W)/\partial M$ for both configurations. We find negative values in the recirculating bubble of the afterbody flow, in a region limited to the internal periphery of the separation line. An increase in the Mach number therefore induces a moderate increase in the backflow velocity, a result consistent with the fact that the modification of the streamwise momentum component weakens the advection of the perturbations. Results are somewhat similar for the sphere, but the negative values found in the recirculating bubble are seen to be larger by one order of magnitude, so that the backflow velocity now strongly increases with the Mach number. Such a difference may be explained by the blockage effect induced by both geometries, which is somewhat limited for the high-aspect ratio afterbody but large for the sphere. In return, the corresponding destabilizing effect is expected to be larger for the sphere, consistent with the results discussed from table 2.

A similar analysis can be carried out for the cross-stream momentum component, which shows that the stabilizing effect is due to an increase in the cross-stream velocity in the recirculating bubble (not shown here for conciseness), the latter being responsible for the strengthening of the cross-stream advection mechanism. In closing this section, it should be noted that the momentum variations found along the separation lines, namely $\partial(\rho W)/\partial M \leqslant 0$ and $\partial(\rho U)/\partial M \geqslant 0$, also mean that the recirculation bubble of the base flow extends as the Mach number increases, as illustrated in figure 11 where we present the evolution of the recirculation length. This may be understood by recalling that the low-pressure levels prevailing in the recirculation bubble limit its spatial extension. When increasing the Mach number, this

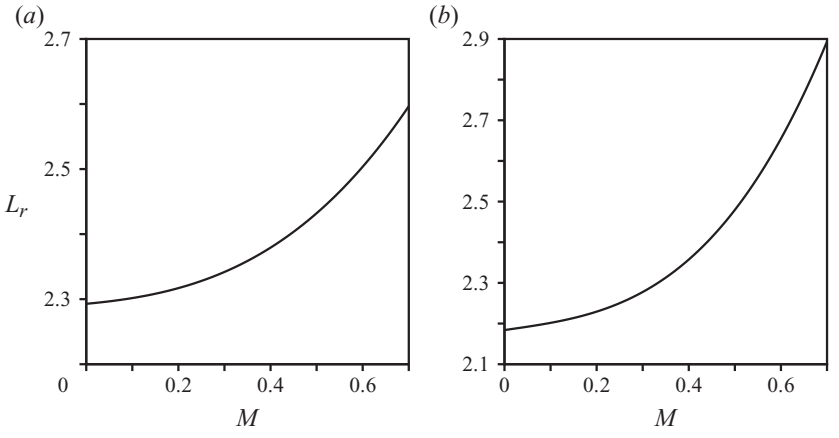

FIGURE 11. Recirculation length L_r of the base flow computed as a function of the Mach number, the Reynolds number being kept constant and equal to its critical value at $M = 0.5$: (*a*) afterbody, $Re_2 = 998.5$; (*b*) sphere, $Re_2 = 275.2$.

effect is relaxed as $1/\gamma M^2$ decreases, hence explaining the increase in the recirculation length. This mechanism persists at high Reynolds numbers, as Merz, Page & Przirembel (1978) earlier reported a similar increase in the recirculation length of the turbulent mean flow developing past an axisymmetric afterbody. The results presented here are therefore believed to be valid also for turbulent flows, at least qualitatively. The importance of the recirculation length on the stability of compressible flows has been briefly discussed by Bouhadji & Braza (2003), who carried out direct numerical simulations of the wake developing past a two-dimensional NACA 0012 wing at zero angle of attack and at a Reynolds number of 10 000. These authors report that the flow is steady at $M = 0$ but that vortex shedding can be triggered by simply increasing the Mach number, an effect that they have attributed to the increase of the recirculation length. Our results question this interpretation since we show that the flow stability properties are different for the afterbody and the sphere, even though the recirculation length increases in both cases. As a result, the variation of the recirculation length must not be seen as the leading mechanism involved in these complex compressible effects, but rather as a systematical consequence of the base flow modification itself. In return, the flow can be either stabilized or destabilized, depending on the competition between the strenghs of the stabilizing cross-stream and destabilizing streamwise advection mechanisms, as sketched in figure 12.

6. Conclusion

A theoretical framework for the study of global modes in compressible flows has been developed and applied to strongly non-parallel axisymmetric wake flows in the high subsonic regime. The base flow, stability and adjoint stability equations have been derived and numerically solved for an axisymmetric blunt-based afterbody modelling an ideal rocket shape and a sphere. A consistent sequence has been found for the destabilization of the steady, axisymmetric solution, that does not depend on the value of the Mach number. A first instability occurs for a stationary global mode (named mode 1) of azimuthal wavenumber $m = 1$, and a second instability occurs at a larger Reynolds number, for an oscillating global mode (named mode 2), of the same azimuthal wavenumber $m = 1$. The similarity between this sequence of destabilization

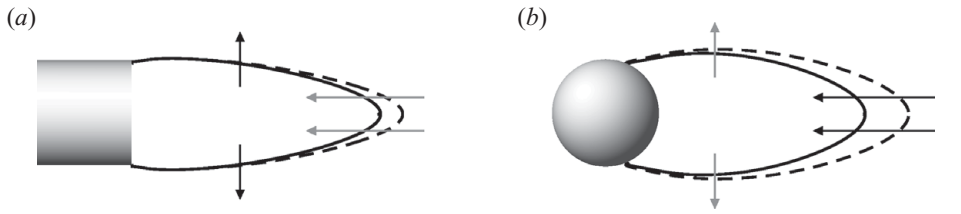

FIGURE 12. Effect of the Mach number on the advection of disturbances for the (*a*) afterbody and (*b*) sphere. The solid and dashed lines delimit the recirculation bubbles for Mach numbers M and $M + \delta M$, respectively. The arrows indicate the direction in which advection of disturbances is strengthened, the dominant contribution being shown as the black arrow.

and the one known from the incompressible flow past a disk and a sphere gives credence to the interpretation of the large-scale oscillation observed in this class of flows at large Reynolds numbers in terms of a global instability triggered by the destabilization of the oscillating mode 2.

The boundaries separating the stable and unstable domains in the (M, Re) plane have been determined, and it has been shown that increasing the Mach number has a stabilizing effect on mode 2 in the case of the blunt-based afterbody. As an attempt to generalize such results to other configurations of axisymmetric wakes, we have computed the same stability boundary for the sphere configuration, and have shown that a similar increase in the Mach number now yields a destabilization of mode 2. This complex stabilizing/destabilizing effect has been further investigated using adjoint-based sensitivity analyses, aimed at predicting the variations of the eigenvalue with the Mach number. The key point here is that compressible effects are simultaneously at work at the base flow and at the perturbation level. The eigenvalue variation arising from both contributions has been derived analytically, and we have shown that the observed compressible effects are triggered by a modification of the base flow profiles. Using this adjoint-based theoretical formalism, a physical interpretation has been proposed, based on a competition between the terms of production, cross-stream advection and streamwise advection. The proposed decomposition provides evidence linking the dominant compressible effect to the modification of the streamwise momentum profiles. If blockage effects are large, an increase in the Mach number strongly strengthens the backflow velocity in the recirculating bubble and makes it able to oppose the downstream advection of disturbances, hence explaining the overall destabilizing effect found for the sphere.

The authors acknowledge financial support of CNES (the French Space Agency) within the framework of the research and technology programme Aerodynamics of Nozzles and Afterbodies.

Appendix A. Sensitivity results to mesh spacing

Seven different meshes, denoted M_1 to M_7 have been used to assess convergence in the numerical results. These meshes, detailed in table 3, exhibit various spatial extents and vertex densities, as well as various sizes for the sponge zones. Results presented in this appendix correspond to the finest mesh M_1. A comparison of the results obtained with the meshes M_1 to M_7 is provided in table 4 and shows that a good convergence is already achieved for the coarser mesh M_6, as results are identical down to the third digit.

	$z_{-\infty}$	z_{∞}	r_{∞}	l^s	n_t	DoF_0	DoF_m
M_1	−100	200	25	100	662 816	2 664 620	3 662 183
M_2	−100	150	25	100	631 559	2 539 022	3 489 557
M_3	−70	200	25	100	653 569	2 627 322	3 610 937
M_4	−100	200	20	100	642 370	2 582 908	3 549 820
M_5	−100	200	25	70	644 067	2 589 454	3 558 851
M_6	−100	200	25	100	441 227	1 774 726	2 439 021
M_7	−100	200	25	100	662 816	2 664 620	3 662 183

TABLE 3. Properties of the meshes as a function of the parameters $z_{-\infty}$, z_{∞}, r_{∞} and l^s, corresponding to the location of the physical inlet, outlet and lateral boundaries, and to the size of the sponge zone: n_t is the number of triangles, DoF_0 is the number of degrees of freedom for axisymmetric state vectors used in the base flow calculations, and DoF_m is the number of degrees of freedom for three-dimensional state vectors used in the global stability calculations. Meshes M_1 and M_2 have the same vertex densities but differ in the location of the outlet boundary. In the same way, M_1 and M_3 differ in the location of the inlet boundary, while M_1 and M_4 differ in the location of the lateral boundary and M_1 and M_5 differ in the size of the sponge zone. M_1 and M_6 have the same spatial extent but M_6 is built with lower vertex densities. M_1 and M_7 are identical but we use a different damping function in the sponge zone, defined by (2.7) along with $\alpha = 3$.

	σ_1	σ_2	ω_2
M_1	7.0×10^{-5}	1.0×10^{-5}	0.3936
M_2	-7.7×10^{-5}	-1.4×10^{-4}	0.3931
M_3	-1.1×10^{-4}	-1.9×10^{-4}	0.3930
M_4	-3.9×10^{-5}	-1.4×10^{-4}	0.3931
M_5	-6.2×10^{-5}	-1.0×10^{-4}	0.3931
M_6	4.6×10^{-5}	2.8×10^{-5}	0.3935
M_7	7.0×10^{-5}	1.0×10^{-5}	0.3936

TABLE 4. Dependence of the eigenvalues on the different meshes characterized in table A. The eigenvalue σ_1 corresponding to the stationary mode 1 is computed at the first instability threshold ($Re_A = 212.6 - M = 0.1$), and the eigenvalue $\sigma_2 + i\omega_2$ corresponding to the oscillating mode 2 is computed at the second instability threshold ($Re_2 = 280.6 - M = 0.1$).

Appendix B. Validation of the adjoint-based gradients

This appendix aims to assess the accuracy of the adjoint method presented in this study. We recall that the variation of a given eigenvalue $\delta\lambda$ is expressed as $\delta\lambda = \delta_{\boldsymbol{Q}}\lambda + \delta_M\lambda$ where $\delta_{\boldsymbol{Q}}\lambda$ and $\delta_M\lambda$ are respectively the variation arising from the modification of the base flow (the Mach number in the perturbation equations being kept constant) and that arising from the modification of the Mach number in the perturbation equations (the base flow being kept constant).

Only the afterbody configuration is considered here. Since the sensitivity analysis is linear in essence, the variation of the eigenvalue computed using the adjoint-based gradients should agree with direct eigenvalue calculation carried out in the limit $\delta M \to 0$. Considering the oscillating global mode 2 at the threshold of the second instability, i.e. $Re_2 = 998.5$ and $M = 0.5$, we compute the linear estimation of the growth rate for different values of δM, thanks to expressions (4.4)–(4.8). These variations are then computed exactly by carrying out the following eigenvalue calculations: assume $\boldsymbol{Q}_1$ is the base flow solution at the Mach number M. For each value of δM, we compute first the base flow $\boldsymbol{Q}_2$, solution of the nonlinear equations

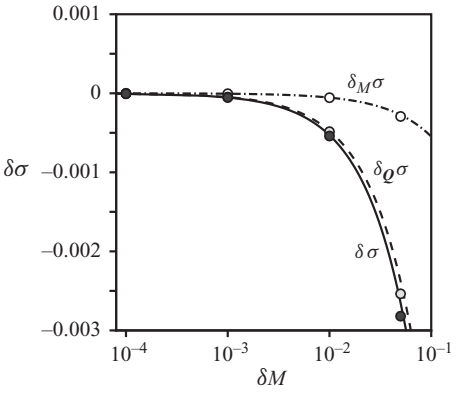

FIGURE 13. Oscillating mode 2 at the threshold of instability, $Re_2 = 998.5 - M = 0.5$: variation of the growth rate as a function of the modification of the Mach number δM. The solid, dashed and dash-dotted lines stand for the variations $\delta\sigma$, $\delta_{\boldsymbol{Q}}\sigma$ and $\delta_M\sigma$ obtained from the sensitivity analysis. The dark grey, light grey and white circle symbols stand for the nonlinear results obtained from direct stability calculations.

(3.1) for the Mach number $M + \delta M$. We solve then numerically the stability problems

$$\delta\lambda \longrightarrow (\lambda + \delta\lambda)\mathscr{B}(\boldsymbol{Q}_2)\hat{\boldsymbol{q}} + \mathscr{A}_m(\boldsymbol{Q}_2, M + \delta M)\hat{\boldsymbol{q}} = \boldsymbol{0}, \tag{B 1a}$$

$$\delta_{\boldsymbol{Q}}\lambda \longrightarrow (\lambda + \delta_{\boldsymbol{Q}}\lambda)\mathscr{B}(\boldsymbol{Q}_2)\hat{\boldsymbol{q}} + \mathscr{A}_m(\boldsymbol{Q}_2, M)\hat{\boldsymbol{q}} = \boldsymbol{0}, \tag{B 1b}$$

$$\delta_M\lambda \longrightarrow (\lambda + \delta_M\lambda)\mathscr{B}(\boldsymbol{Q}_1)\hat{\boldsymbol{q}} + \mathscr{A}_m(\boldsymbol{Q}_1, M + \delta M)\hat{\boldsymbol{q}} = \boldsymbol{0}, \tag{B 1c}$$

the associated growth rate variations being obtained simply by retaining the real parts.

Figure 13(*a*) depicts the growth rate variations computed as functions of the amplitude δM. The dark grey symbols (resp. light grey and white circle symbols) stand for the exact nonlinear variation $\delta\sigma$ (resp. $\delta_Q\sigma$ and $\delta_M\sigma$) obtained by direct stability calculations. The corresponding linear estimations arising from the sensitivity analysis are presented as the solid, dashed and dash-dotted curves, respectively. For small amplitudes $\delta M < 10^{-3}$, the relative difference is not measurable and results are superposed, indicating that the base flow modification owing to the increase in M is linear in this range. These results validate the sensitivity analysis and in particular the accuracy of the sensitivity functions computed in this study. For larger amplitudes, we observe small discrepancies, as the decrease in the growth rate is slightly larger if computed by stability calculations. This means that the true nonlinear stabilizing effect of the Mach number is slightly larger than that estimated by the sensitivity analysis. Still, the variations obtained up to $\delta M = 0.05$ are very well approximated by the linear estimation, as the maximum relative difference is about 6 %.

Appendix C. Derivation of the sensitivity functions to base flow modifications

The eigenvalue variation $\delta_{\boldsymbol{Q}}\lambda$, simply noted $\delta\lambda$ here to ease the notation, is investigated with respect to the base flow modification $\boldsymbol{\delta Q}$, the Mach number being kept constant. The variations are such that

$$\delta\lambda = \delta\sigma + \mathrm{i}\delta\omega = \langle \boldsymbol{\nabla}_{\boldsymbol{Q}}\lambda\,,\, \boldsymbol{\delta Q}\rangle, \tag{C 1}$$

where we use from now on $\langle \hat{\boldsymbol{a}}\,, \hat{\boldsymbol{b}}\rangle = \displaystyle\int_\Omega \hat{\boldsymbol{a}}\cdot\hat{\boldsymbol{b}}\, r\, \mathrm{d}\Omega$ for compact notation.

In the present formalism, the base flow $\boldsymbol{Q}$ is the control variable, the eigenpair $\{\hat{\boldsymbol{q}}, \lambda\}$ is the state variable and eigenproblem (3.3) is the state equation, i.e. the constraint to be satisfied. We introduce a Lagrange multiplier $\hat{\boldsymbol{q}}^\dagger$ (also known as 'adjoint' or 'co-state' variable) for the state variable, now referred to as the adjoint perturbation, and define the functional

$$\mathscr{L}(\boldsymbol{Q}, \hat{\boldsymbol{q}}^\dagger, \hat{\boldsymbol{q}}, \lambda) = \lambda - \langle \hat{\boldsymbol{q}}^\dagger , \lambda \mathscr{B}(\boldsymbol{Q})\hat{\boldsymbol{q}} + \mathscr{A}_m(\boldsymbol{Q})\hat{\boldsymbol{q}} \rangle. \tag{C 2}$$

The gradient, with respect to any variable s, is defined as

$$\frac{\partial \mathscr{L}}{\partial s}\delta s = \lim_{\epsilon \to 0} \frac{\mathscr{L}(s + \epsilon \delta s) - \mathscr{L}(s)}{\epsilon}. \tag{C 3}$$

We assume that the state equation is satisfied for any arbitrary base flow modification, so that the gradient of the functional with respect to the adjoint variable is zero. It can be checked that the gradient with respect to the state variable is zero, provided we define $\hat{\boldsymbol{q}}^\dagger$ as the solution of the adjoint eigenvalue problem

$$\lambda^* \mathscr{B}^\dagger(\boldsymbol{Q})\hat{\boldsymbol{q}}^\dagger + \mathscr{A}_m^\dagger(\boldsymbol{Q})\hat{\boldsymbol{q}}^\dagger = \boldsymbol{0}, \tag{C 4}$$

along with the normalization condition (4.2). In (C 4), $\mathscr{B}^\dagger$ and $\mathscr{A}_m^\dagger$ are the adjoint of operators $\mathscr{B}$ and $\mathscr{A}_m$, obtained by integrating by parts the disturbance equations (Schmid & Henningson 2001). We obtain simply $\mathscr{B}^\dagger = \mathscr{B}$ since $\mathscr{B}$ is a diagonal operator, whereas the complete expression of operator $\mathscr{A}_m^\dagger$ can be found in Appendix D. The boundary conditions to be fulfilled by the adjoint perturbations are such that all boundary terms arising during the integration by part vanish, which imposes conditions identical to that of the global modes. Eigenproblem (C 4) is solved via the Arnoldi method, and adjoint global modes are then normalized with respect to the direct global modes, according to (4.2). Since this adjoint problem is formulated for continuous operators, the spatial discretization of operators $\mathscr{A}_m$ and $\mathscr{A}_m^\dagger$ leads to discrete operators that are not Hermitian conjugates. Consequently, we check *a posteriori* that the adjoint eigenvalues are complex conjugate with the direct eigenvalues and that a bi-orthogonality relation is satisfied for the 10 leading global modes (i.e. that the scalar product of one of the 10 leading adjoint modes with any of the 10 leading direct global modes is less than 10^{-6}, except when the direct and adjoint modes correspond to complex conjugate eigenvalues), and conclude that our numerical procedure accurately estimates the direct and adjoint global modes of the compressible problem.

The eigenvalue variation now reads

$$\delta\lambda = \frac{\partial \mathscr{L}}{\partial \boldsymbol{Q}}\boldsymbol{\delta Q}. \tag{C 5}$$

The gradient of the functional with respect to the base flow can be expressed as

$$\begin{aligned} \frac{\partial \mathscr{L}}{\partial \boldsymbol{Q}}\boldsymbol{\delta Q} &= \left\langle -\hat{\boldsymbol{q}}^\dagger , \frac{\partial}{\partial \boldsymbol{Q}}(\lambda \mathscr{B}(\boldsymbol{Q})\hat{\boldsymbol{q}} + \mathscr{A}_m(\boldsymbol{Q})\hat{\boldsymbol{q}})\boldsymbol{\delta Q} \right\rangle \\ &= -\left\langle \left\{ \frac{\partial}{\partial \boldsymbol{Q}}(\lambda \mathscr{B}(\boldsymbol{Q})\hat{\boldsymbol{q}} + \mathscr{A}_m(\boldsymbol{Q})\hat{\boldsymbol{q}}) \right\}^\dagger \hat{\boldsymbol{q}}^\dagger , \boldsymbol{\delta Q} \right\rangle, \end{aligned} \tag{C 6}$$

so that the sensitivity function $\nabla_{\boldsymbol{Q}}\lambda$ is given by

$$\nabla_{\boldsymbol{Q}}\lambda = -\left\{ \frac{\partial}{\partial \boldsymbol{Q}}(\lambda \mathscr{B}(\boldsymbol{Q})\hat{\boldsymbol{q}} + \mathscr{A}_m(\boldsymbol{Q})\hat{\boldsymbol{q}}) \right\}^\dagger \hat{\boldsymbol{q}}^\dagger. \tag{C 7}$$

Because we use non-conservative variables in the numerics, expression (C 7) corresponds to the sensitivity function $\nabla_{\boldsymbol{Q}}\lambda = (\nabla_\rho\lambda, \nabla_{\boldsymbol{U}}\lambda, \nabla_T\lambda, \nabla_P\lambda)^T$, where $\nabla_\rho\lambda$, $\nabla_{\boldsymbol{U}}\lambda$, $\nabla_T\lambda$ and $\nabla_P\lambda$ define the sensitivity of the eigenvalue to a small modification of the base flow density, velocity, temperature and pressure, such that

$$\delta\lambda = \int_\Omega \left(\nabla_\rho\lambda\cdot\delta\rho + \nabla_{\boldsymbol{U}}\lambda\cdot\boldsymbol{\delta U}) + \nabla_T\lambda\cdot\delta T + \nabla_P\lambda\cdot\delta P\right) r\,\mathrm{d}\Omega. \tag{C 8}$$

To derive the sensitivity functions in term of the conservative variables, as defined by (4.9), we simply substitute $\boldsymbol{\delta Q}$ by its conservative counterpart $\mathscr{H}\boldsymbol{\delta Q}$ into (C 6), since both relations (4.7) and (C 8) are to be simultaneously satisfied.

In closing this section, it should be noted that such an approach is very similar to that used in optimization problems, where one enforces the stationarity of a Lagrangian as a means to minimize a given functional under specific constraint. We would like to insist that no such stationarity is enforced here, and that the functional is only used as a means to compute the different gradients of interest.

Appendix D. Detailed expression of the differential operators

All operators given here pertain to the complete state vector $\boldsymbol{q} = (\rho, \boldsymbol{u}, T, p)^T$. The reduced form of these operators, i.e. that pertaining to the state vector $\boldsymbol{q} = (\rho, \boldsymbol{u}, T)^T$ used in the numerics, can be straightforwardly obtained by replacing the pressure terms by their expressions arising from the perfect gas state equation. The solid symbols $\bullet$ are used to clarify the action of a selected number of differential operators. $\mathscr{I}$ being the identity operator, the non-zero terms of operators $\mathscr{B}$, $\mathscr{A}_m$ and $\mathscr{C}_m$ describing the evolution of the global modes are

$$\begin{aligned}
\mathscr{B}_{11} &= 1,\\
\mathscr{B}_{22} &= \rho\mathscr{I},\\
\mathscr{B}_{33} &= \rho,
\end{aligned}$$

$$\begin{aligned}
\mathscr{A}_{m11} &= \boldsymbol{U}\cdot\nabla + \nabla\cdot\boldsymbol{U},\\
\mathscr{A}_{m12} &= \nabla\rho\cdot + \rho\nabla,\\
\mathscr{A}_{m21} &= \nabla\boldsymbol{U}\cdot\boldsymbol{U},\\
\mathscr{A}_{m22} &= \rho\nabla[\bullet]\cdot\boldsymbol{U} + \rho\nabla\boldsymbol{U}\cdot[\bullet] - \frac{1}{Re}\nabla\cdot\boldsymbol{\tau}[\bullet],\\
\mathscr{A}_{m24} &= \frac{1}{\gamma M^2}\nabla,\\
\mathscr{A}_{m31} &= \boldsymbol{U}\cdot\nabla T,\\
\mathscr{A}_{m32} &= \rho\nabla T\cdot + (\gamma-1)P\nabla\cdot - \gamma(\gamma-1)\frac{M^2}{Re}\left(\boldsymbol{\tau}(\boldsymbol{U}):\boldsymbol{d}[\bullet] + \boldsymbol{\tau}[\bullet]:\boldsymbol{d}(\boldsymbol{U})\right),\\
\mathscr{A}_{m33} &= \rho\boldsymbol{U}\cdot\nabla - \frac{\gamma}{Pr\,Re}\nabla^2,\\
\mathscr{A}_{m34} &= (\gamma-1)\nabla\cdot\boldsymbol{U},\\
\mathscr{A}_{m41} &= -T,\\
\mathscr{A}_{m43} &= -\rho,\\
\mathscr{A}_{m44} &= 1,
\end{aligned}$$

$$\mathscr{C}_{m11} = \boldsymbol{U}\cdot\nabla + \nabla\cdot\boldsymbol{U},$$
$$\mathscr{C}_{m21} = \nabla\boldsymbol{U}\cdot\boldsymbol{U},$$
$$\mathscr{C}_{m22} = \rho\nabla[\bullet]\cdot\boldsymbol{U},$$
$$\mathscr{C}_{m31} = \boldsymbol{U}\cdot\nabla T,$$
$$\mathscr{C}_{m33} = \rho\boldsymbol{U}\cdot\nabla.$$

Similarly, the non-zero terms of the adjoint operators $\mathscr{A}_m^\dagger$ and $\mathscr{C}_m^\dagger$ are

$$\mathscr{A}_{m11}^\dagger = -\boldsymbol{U}\cdot\nabla,$$
$$\mathscr{A}_{m12}^\dagger = (\nabla\boldsymbol{U}\cdot\boldsymbol{U})\cdot,$$
$$\mathscr{A}_{m13}^\dagger = \boldsymbol{U}\cdot\nabla T,$$
$$\mathscr{A}_{m14}^\dagger = -T,$$
$$\mathscr{A}_{m21}^\dagger = -\rho\nabla,$$
$$\mathscr{A}_{m22}^\dagger = -\rho\nabla[\bullet]\cdot\boldsymbol{U} + \rho\nabla\boldsymbol{U}^T\cdot - \frac{1}{Re}\nabla\cdot\boldsymbol{\tau}[\bullet],$$
$$\mathscr{A}_{m23}^\dagger = \rho\nabla T - (\gamma-1)\nabla(P[\bullet]) + 2\gamma(\gamma-1)\frac{M^2}{Re}\nabla\cdot([\bullet]\boldsymbol{\tau}(\boldsymbol{U})),$$
$$\mathscr{A}_{m33}^\dagger = -\rho\boldsymbol{U}\cdot\nabla - \frac{\gamma}{PrRe}\nabla^2,$$
$$\mathscr{A}_{m34}^\dagger = -\rho,$$
$$\mathscr{A}_{m42}^\dagger = -\frac{1}{\gamma M^2}\nabla\cdot,$$
$$\mathscr{A}_{m43}^\dagger = (\gamma-1)\nabla\cdot\boldsymbol{U},$$
$$\mathscr{A}_{m44}^\dagger = 1\,,$$

$$\mathscr{C}_{m11}^\dagger = -\boldsymbol{U}\cdot\nabla,$$
$$\mathscr{C}_{m12}^\dagger = (\nabla\boldsymbol{U}\cdot\boldsymbol{U})\cdot,$$
$$\mathscr{C}_{m13}^\dagger = \boldsymbol{U}\cdot\nabla T,$$
$$\mathscr{C}_{m22}^\dagger = -\rho\nabla[\bullet]\cdot\boldsymbol{U},$$
$$\mathscr{C}_{m33}^\dagger = -\rho\boldsymbol{U}\cdot\nabla.$$

REFERENCES

Achenbach, E. 1972 Experiments on the flow past spheres at very high Reynolds numbers. *J. Fluid Mech.* **54**, 565–575.

Achenbach, E. 1974 Vortex shedding from spheres. *J. Fluid Mech.* **62**, 209–221.

Barkley, D., Gomes, M. G. M. & Henderson, R. D. 2002 Three-dimensional instability in flow over a backward-facing step. *J. Fluid Mech.* **473**, 167–190.

Bottaro, A., Corbett, P. & Luchini, P. 2003 The effect of base flow variation on flow stability. *J. Fluid Mech.* **476**, 293–302.

Bouhadji, A. & Braza, M. 2003 Physical analysis by numerical simulation of organised modes and shock-vortex interaction in transonic flows around an aerofoil. Part 1. Mach number effect. *J. Comput. Fluids* **32**, 1233–1260.

Brès, G. A. & Colonius, T. 2008 Three-dimensional instabilities in compressible flow over open cavities. *J. Fluid Mech.* **599**, 309–339.

Chomaz, J.-M. 2005 Global instabilities in spatially developing flows: non-normality and nonlinearity. *Annu. Rev. Fluid. Mech.* **37**, 357–392.

Colonius, T. 2004 Modeling artificial boundary conditions for compressible flow. *Annu. Rev. Fluid Mech.* **36**, 315–345.

Corbett, P. & Bottaro, A. 2000 Optimal perturbations for boundary layers subject to streamwise pressure gradient. *Phys. Fluids* **12**, 120–130.

Corbett, P. & Bottaro, A. 2001 Optimal control of nonmodal disturbances in boundary layers. *Theor. Comput. Fluid Dyn.* **15**, 65–81.

Crouch, J. D., Garbaruk, A. & Magidov, D. 2007 Predicting the onset of flow unsteadiness based on global instability. *J. Comput. Phys.* **224**, 924–940.

Crouch, J. D., Garbaruk, A., Magidov, D. & Travin, A. 2009 Origin of transonic buffet on aerofoils. *J. Fluid Mech.* **628**, 357–369.

Davis, T. A. 2004 A column pre-ordering strategy for the unsymmetric-pattern multifrontal method. *ACM Trans. Math. Softw.* **30** (2), 165–195.

Davis, T. A. & Duff, I. S. 1997 An unsymmetric-pattern multifrontal method for sparse LU factorization. *SIAM J. Matrix Anal. Appl.* **18** (1), 140–158.

Deprés, D., Reijasse, P. & Dussauge, J.-P. 2004 Analysis of unsteadiness in afterbody transonic flows. *AIAA J.* **42** (12), 2541–2550.

Ehrenstein, U. & Gallaire, F. 2005 On two-dimensional temporal modes in spatially evolving open flows: the flat-plate boundary layer. *J. Fluid Mech.* **536**, 209–218.

Fabre, D., Auguste, F. & Magnaudet, J. 2008 Bifurcations and symmetry breaking in the wake of axisymmetric bodies. *Phys. Fluids* **20** (5), 051702.

Fuchs, H. V., Mercker, E. & Michel, U. 1979 Large-scale coherent structures in the wake of axisymmetric bodies. *J. Fluid Mech.* **93**, 185–207.

Giannetti, F. & Luchini, P. 2003 Receptivity of the circular cylinders first instability. In *Proceedings of 5th European Fluid Mechanics Conference*, Toulouse, France.

Giannetti, F. & Luchini, P. 2007 Structural sensitivity of the first instability of the cylinder wake. *J. Fluid Mech.* **581**, 167–197.

Gunzburger, M. D. 1999 Sensitivities, adjoints and flow optimization. *Intl J. Numer. Math. Fluids* **31** (1), 53–78.

Hwang, Y. & Choi, H. 2006 Control of absolute instability by basic-flow modification in parallel wake at low Reynolds number. *J. Fluid Mech.* **560**, 465–475.

Jackson, C. P. 1987 A finite-element study of the onset of vortex shedding in flow past variously shaped bodies. *J. Fluid Mech.* **182**, 23–45.

Jackson, T. L. & Grosch, C. E. 1990 Absolute/convective instabilities and the convective Mach number in a compressible mixing layer. *Phys. Fluids* A **2**, 949–954.

Jendoubi, S. & Strykowski, P. J. 1994 Absolute and convective instability of axisymmetric jets with external flow. *Phys. Fluids* **6** (9), 3000–3009.

Johnson, T. A. & Patel, V. C. 1999 Flow past a sphere up to a Reynolds number of 300. *J. Fluid Mech.* **378**, 19–70.

Lesshafft, L. & Huerre, P. 2007 Linear impulse response in hot round jets. *Phys. Fluids* **19** (2), 024102.

Luchini, P. & Bottaro, A. 1998 Görtler vortices: a backward-in-time approach to the receptivity problem. *J. Fluid Mech.* **363**, 1–23.

Mack, C. J., Schmid, P. J. & Sesterhenn, J. L. 2008 Global stability of swept flow around a parabolic body: connecting attachment-line and crossflow modes. *J. Fluid Mech.* **611**, 205–214.

Mair, W. A. 1965 The effect of a rear-mounted disc on the drag of a blunt-based body of revolution. *Aeronaut. Q.* **16**, 350–360.

Marquet, O., Lombardi, M., Chomaz, J.-M., Sipp, D. & Jacquin, L. 2009 Direct and adjoint global modes of a recirculation bubble: lift-up and convective non-normalities. *J. Fluid Mech.* **622**, 1–21.

Marquet, O., Sipp, D. & Jacquin, L. 2008 Sensitivity analysis and passive control of the cylinder flow. *J. Fluid Mech.* **615**, 221–252.

Matsumoto, J. & Kawahara, M. 2000 Stable shape identification for fluid–structure interaction problem using MINI element. *J. Appl. Mech.* **3**, 263–274.

Meliga, P., Chomaz, J.-M. & Sipp, D. 2009*a* Global mode interaction and pattern selection in the wake of a disk: a weakly nonlinear expansion. *J. Fluid. Mech.* **633**, 159–189.

Meliga, P., Chomaz, J.-M. & Sipp, D. 2009*b* Unsteadiness in the wake of disks and spheres: instability, receptivity and control using direct and adjoint global stability analyses. *J. Fluid. Struc.* **25**, 601–616.

Meliga, P., Sipp, D. & Chomaz, J.-M. 2008 Absolute instability in axisymmetric wakes: compressible and density variation effects. *J. Fluid Mech.* **600**, 373–401.

Merz, R. A., Page, R. H. & Przirembel, C. E. G. 1978 Subsonic axisymmetric near-wake studies. *AIAA J.* **16**, 656–662.

Michalke, A. 1971 Instabilität eines kompressiblen runden Freistrahls unter Berücksichtigung des Einflusses der Strahlgrenzschichtdicke. *Z. Plugwiss.* (19), 319–328 (English translation in NASA TM 75190, 1977).

Monkewitz, P. A. & Sohn, K. D. 1988 Absolute instability in hot jets. *AIAA J.* **26** (8), 911–916.

Natarajan, R. & Acrivos, A. 1993 The instability of the steady flow past spheres and disks. *J. Fluid Mech.* **254**, 323–344.

Nichols, J. W., Schmid, P. J. & Riley, J. J. 2007 Self-sustained oscillations in variable-density round jets. *J. Fluid Mech.* **582**, 341–376.

Ormières, D. & Provansal, M. 1999 Transition to turbulence in the wake of a sphere. *Phys. Rev. Lett.* **83**, 80–83.

Pavithran, S. & Redekopp, L. G. 1989 The absolute-convective transition in subsonic mixing layers. *Phys. Fluids* A **1** (10), 1736–1739.

Robinet, J.-C. 2007 Bifurcations in shock-wave/laminar-boundary layer interaction: global instability approach. *J. Fluid Mech.* **579**, 85–112.

Schlichting, H. 1978 *Boundary Layer Theory*, 7th edn. McGraw-Hill.

Schmid, P. J. & Henningson, D. S 2001 *Stability and Transition in Shear Flows*. Springer.

Seidel, J., Siegel, S., Jeans, T., Aradag, S., Cohen, K. & McLaughlin, T. 2008 Analysis of an axisymmetric bluff body wake using Fourier transform and POD. *AIAA Paper* 2008-552.

Sevilla, A. & Martínez-Bazàn, C. 2004 Vortex shedding in high Reynolds number axisymmetric bluff-body wakes: local linear instability and global bleed control. *Phys. Fluids* **16** (9), 3460–3469.

Siegel, S. G. & Fasel, H. F. 2001 Effect of forcing on the wake drag of an axisymmetric bluff body. *AIAA Paper* 2001-0736.

Siegel, S., Seidel, J., Cohen, K., Aradag, S. & McLaughlin, T. 2008 Open loop transient forcing of an axisymmetric bluff body wake. *AIAA Paper* 2008-595.

Soteriou, M. C. & Ghoniem, A. F. 1995 Effects of the free-stream density ratio on free and forced spatially developing shear layers. *Phys. Fluids* **7** (8), 2036–2051.

Taneda, S. 1978 Visual observations of the flow past a sphere at Reynolds numbers between 10^4 and 10^6. *J. Fluid Mech.* **85**, 187–192.

Tomboulides, A. G. & Orszag, S. A. 2000 Numerical investigation of transitional and weak turbulent flow past a sphere. *J. Fluid Mech.* **416**, 45–73.

Weickgenannt, A. & Monkewitz, P. A. 2000 Control of vortex shedding in an axisymmetric bluff body wake. *Eur. J. Mech.* B *Fluids* **19**, 789–812.